



POLITEHNICA UNIVERSITY OF BUCHAREST



Doctoral School on Engineering and Applications of Lasers and Accelerators

Decision No. _____ from _____

Ph.D. THESIS SUMMARY

Dragos-Florian NICHITA

RADIOACTIVE ION BEAMS DRIVEN BY γ -RAYS INDUCED
FISSION OF ^{238}U AND PROMPT FISSION γ -RAYS IN $^{233}\text{U}(\text{n}_{\text{th}},\text{f})$

THESIS COMMITTEE

Prof. Dr. Ing. Calin UR Politehnica Univ. of Bucharest & ELI-NP	President
Prof. Dr. Dimiter L. BALABANSKI Politehnica Univ. of Bucharest & ELI-NP	PhD Supervisor
Prof. Dr. Octavian SIMA University of Bucharest & ELI-NP	Referee
Prof. Dr. Anabella TUDORA University of Bucharest	Referee
Prof. Dr. Mieczyslaw W. KRASNY LPNHE Sorbonne University & CERN	Referee

BUCHAREST 2022

”We are like dwarfs sitting on the shoulders of giants. We see more, and things that are more distant, than they did, not because our sight is superior or because we are taller than they, but because they raise us up, and by their great stature add to ours.”

– John of Salisbury, Metalogicon Of John Salisbury –

I want to thank all of my professors and fellow scientists that helped me in the quest of seeing further and understanding deeper. I also want to thank my family and friends for encouraging me to follow my passion for Physics, my need for trying to understand the roots of existence. I do not know what the future will bring but I have greatly enjoyed the trip so far with all of its up and downs. I also would like to remind myself and anyone who reads this that we need to keep an open mind and doubt everything to a rational degree because one big trap that I have encountered in my PhD period is being too sure of certain theories or formalisms, even putting them in the center of our thinking and use them to explain the Universe behavior (e.g. The rules of selection do not allow certain transitions or the Pauli exclusion principle prevent that two identical fermions can simultaneously occupy the same quantum state).

”I cannot teach anybody anything. I can only make them think.”

– Socrates –

Contents

1	Introduction to nuclear fission	5
1.1	General description of nuclear fission	5
1.2	Prompt gamma rays as fission probes	9
1.3	Production of neutron rich fission fragments	9
2	The role of neutron rich nuclei in cosmology	11
2.1	Cosmology and nucleosynthesis	11
2.1.1	Birth of the Universe	11
2.1.2	The formation of the chemical elements	12
2.2	The r -path mechanism in extreme stellar environments	14
2.3	RIB facilities as laboratories for exotic nuclei	16
3	Prompt fission γ-rays in $^{233}\text{U}(\text{n}_{th},\text{f})$	19
3.1	Experimental setup at Budapest Nuclear Reactor	19
3.2	Data analysis	20
3.2.1	Energy calibration and energy resolution	20
3.2.2	Unfolding the recorded data from the detector response function using the matrix inversion method	20
3.2.3	GEANT4 simulations for assessing the detector response .	22
3.2.4	Response matrix calculations	24
4	Photo-fission mechanism for RIB generation	27
4.1	RIB generation driven by CBS gamma beams	27
4.1.1	The ELISOL beamline at ELI-NP	28
4.1.2	Improved photo-fission model	28
4.1.3	Design and optimization of the target system	29
4.1.4	Estimated RIB production yields	31

5	Radioactive ion beam production at the Gamma Factory	33
5.1	The Gamma Factory facility at CERN	33
5.1.1	Project description	33
5.1.2	Beam generation and properties	34
5.1.3	RIB formation with ion catcher	35
5.1.4	Simulation of production rates	37
5.1.5	Extraction efficiency estimation	40
5.1.6	RIB yields available for measurement	43
5.2	Physics opportunities with RIBs at Gamma Factory	45
6	Conclusions and outlook	48

Chapter 1

Introduction to nuclear fission

This chapter has the goal of introducing the main concepts of the nuclear fission process, such that it provides a basis for the work presented later in the thesis.

1.1 General description of nuclear fission

Nuclear fission [1] was discovered in 1938 by Otto Hahn and his colleague Fritz Straßmann when they observed barium (Ba) being created after the heavy uranium nuclei "burst" as they intuitively called it. The nuclear fission is the process in which usually a large (heavy) nucleus undergoes considerable deformation, from which it will not recover, and splits up. This deformation process is related to the nuclear energy states. In fig.1.1 one can observe a sketch of the dependence of the quadrupole deformation parameter (β_2) as a function of the excitation energy in the case of ^{232}U [2], as well as different states and pathways [3] [4] that the nucleus takes along the fission road.

In classical physics terms, a minimum amount of energy is needed to excite the nucleus above the point from which it can undergo fission, with this energy threshold acting like a barrier. In a general case, this barrier has a multi-humped shape which describe the nuclear potential of the system. Any type of interacting particle can add energy to the mother nucleus and induce fission but the most studied type, due to its use in the energetic sector, is the neutron induced one. This is the process in which a neutron interacts and gets absorbed by a fissile nucleus causing an increase in the energy state of that particular nucleus. This added energy can manifest as vibrational and/or rotational energy causing the nucleus to deform and have a greater probability of splitting. That being said, there are

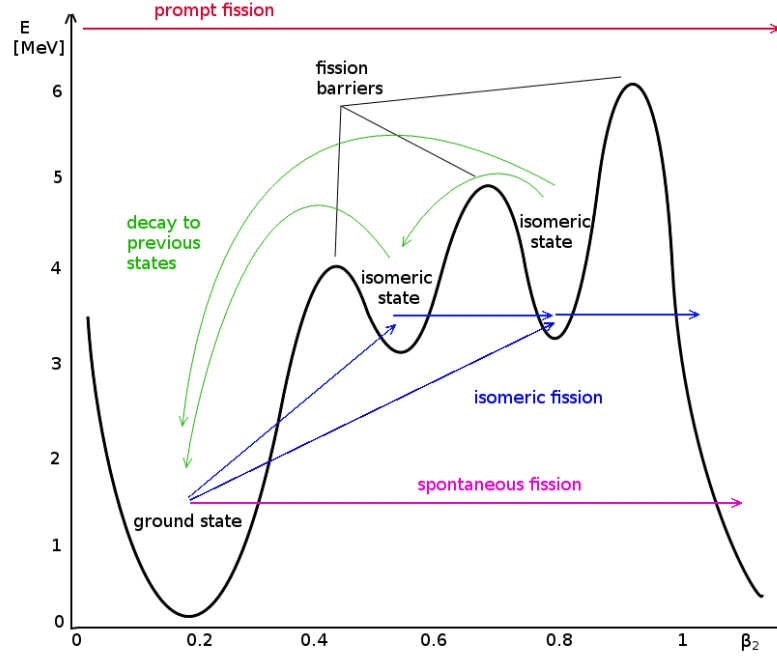


Figure 1.1: Triple-humped fission barrier schematic for ^{232}U . The red arrow shows the potential path to fission in the case of nuclei with an available energy greater than the barrier. The green arrows show the de-excitation and fall-back from higher energy isomeric states to the ground state. The blue arrows shows possible paths towards fission going through shape isomers and the purple arrow show the spontaneous fission case.

effects such as quantum tunneling that can trigger spontaneous fission without any external energy required. The quantum state of each elementary particle of the nucleus plays a role in the state of the whole system such that the whole nucleus behaves according to the quantum mechanical rules being able to decay or tunnel through the potential barrier. Any quantum system has a non-zero probability of being outside of a potential well, which is defined by the square modulus of the wave function at that particular position. Another possible fissioning path, defined by the actual shape of the potential, is isomeric fission, which implies a multi-step process, the system going through isomeric states before splitting.

Independent of the way fission is induced (i.e. neutron, proton, gamma, etc.) or even in the case of spontaneous fission, there are specific steps that the nucleus undergoes. In the literature, this is known as the Bohr independence hypothe-

sis. After a deformation threshold, called the scission point, the nucleus is split into fission fragments (usually two) possessing high kinetic and excitation energy, around 200 MeV per each fissioning act [5]. The mass and charge distribution of the daughter nuclei (A_1, Z_1) and (A_2, Z_2) depends on the fission type, the mother nucleus (A_0, Z_0) and its energy state with the mass and charge conservation $A_1 + A_2 = A_0$ and $Z_1 + Z_2 = Z_0$. An example of distribution for the daughter masses, both light and heavy fission fragments, is shown in fig. 1.2 for the case of photon induced fission of ^{238}U generated with a 14 MeV gamma energy using the GIF model [6].

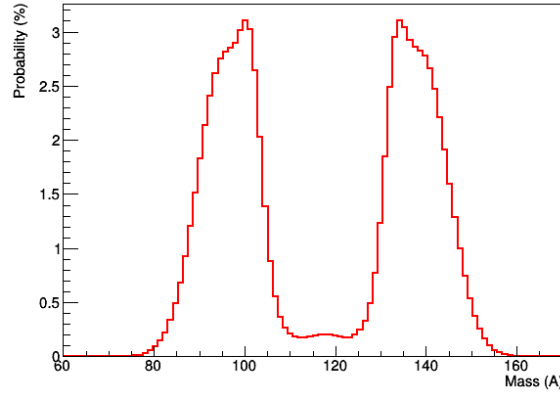


Figure 1.2: Fission fragments mass distribution, generated through 14 MeV photons induced fission, using original code implementation of the GIF model.

The neutron-to-proton (N/Z) ratio rises with the mass number (A), as lighter nuclei usually have equal number of protons and neutrons but heavier nuclei need more neutrons than protons in order to compensate for the long-range Coulomb repulsion occurring between protons, that is summing up. The two fission fragments are much lighter in mass than the mother nucleus and thus the daughter nuclei which retain the (N/Z) ratio will have a larger number of neutrons than the corresponding stable configuration at their specific mass. Because of this, they are called neutron-rich nuclei. Some fission generated nuclei will have an uncommonly high N/Z ratios and that is why they are called exotic neutron-rich nuclei. These last ones are produced with very small probabilities and have usually low lifetimes thus earning the name of exotic nuclei. Being neutron-rich and generated in different excited states, the fission fragments will decay fast and the desired channel is neutron separation, therefore emitting prompt fission neutrons. In competition, the nucleus can decay through other available channels, such as

by emitting gamma rays that are called prompt fission gamma rays. After this prompt phase showed in fig. 1.3 is finalized the fission fragments can emit delayed neutrons and gammas to go to their ground state in competition to the beta minus decay that can occur as a nuclear restructure toward the lowest energy state.

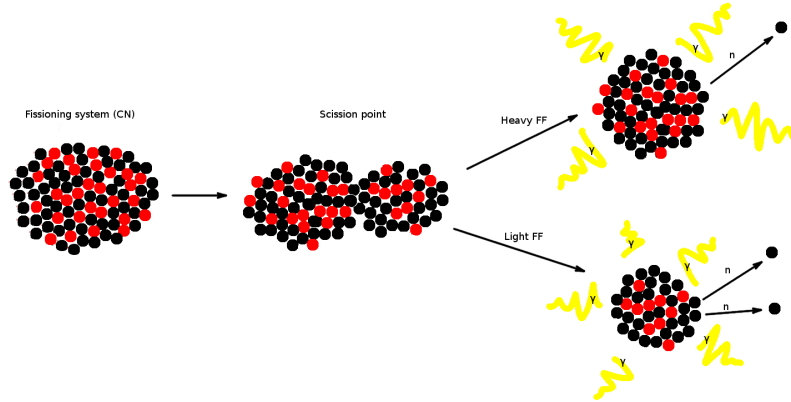


Figure 1.3: Diagram illustrating the prompt fission step in which the mother nucleus splits into one light and one heavy fragments which decay by emitting prompt neutrons (black dots) and gamma rays (yellow zig-zag lines)

The study of the fission process is of importance for the energy production field (i.e. nuclear reactors) but also for the fundamental understanding of the nuclear structure, decay channels, and so on. An important aspect of nuclear fission is also that it can sustain a chain reaction. Each fission process usually generates between two to four neutrons that can each induce fission in another mother nuclei, thus perpetuating the chain reaction. Due to the fact that the neutron emission multiplicity per each fission event is higher than one, the reaction will accelerate exponentially and become uncontrolled as being the case of nuclear weapons. In civilian applications, such as nuclear reactors, a constant reaction rate is needed and thus the emitted neutrons are kept below the critical number by introducing neutron capturing materials such as cadmium in the active reaction zone. In order to better control the fission rate many experiments have been conducted with the goal of determining parameters such as: the energy emitted in the fission process, prompt neutron and gamma multiplicities along with their energy distribution as well as cross sections of interaction channels that lead to nuclear fission. Some of these studies, results or procedures are presented or recalled in the later chapters of this thesis.

1.2 Prompt gamma rays as fission probes

As described in the previous section, after the splitting of the mother nucleus takes place, the generated fission fragments (daughters) are in excited states and will then decay in two phases: the prompt phase (10^{-12} s) and the delayed phase. In the prompt phase the daughter nucleus decays mainly through neutron (prompt neutrons) and gamma emission (prompt gammas). While prompt neutrons have a large impact on the fission chain reaction mechanism and are largely studied especially for the energy generation applications, the prompt gammas carry just a small portion of the released energy and play a minor role in the chain reaction equation, which is why the literature is not so vast [7]. Still the prompt emitted gammas, carry information about the energy states of the daughter nuclei, their electromagnetic decay type, etc, meaning they can be very helpful in fundamental research such as nuclear structure studies but also on residual emitted radiation for different applications such as future generation nuclear reactors. This knowledge can be also used in parallel with fission fragments mass determination for further understanding the details of the fission process itself. The analysis of a prompt fission gamma ray spectrum (PFGS) comes with serious challenges, partially due to the fact that the fission process can generate hundreds of different isotope pairs in many different excited states thus the energy spectrum has a quasi continuum shape with little to no peaks present. On top of this, many other aspects such as the detector response function and performance make the study even more difficult. Some of those challenges and solutions are presented in chapter 3 of this thesis, in a case study experiment.

1.3 Production of neutron rich fission fragments

One of the main ways to gain knowledge in nuclear physics is by observing the behavior of specific nuclei of interest and measuring different probes generated through nuclear reactions. Such observations allowed the development of theoretical nuclear models including: shell model in which nucleons are arranged in shell-like structure similar to the atom and the liquid drop model where the nuclear matter is treated as a liquid-like substance. In order to move forward with the current understanding of the nuclear environment, the research community is trying to observe new bound systems that were not observed up to this point and thus bring new constraints for theoretical models development. As described in previous sections, in the nuclear fission process, following scission, the nuclear

fragments are generated in a wide distribution of masses and charges thus this process can provide the means to produce a high number of combinations of protons and neutrons starting from low ($A \approx 30$) up to higher ($A \approx 200$) masses. Each of these fission fragments, with its specific combination of the number of protons (Z) and number of neutrons (N), is produced with a certain probability. As an example, in fig. 1.4 the production probabilities, normalized to unity, are shown for each isotope in the case of the photon induced fission of ^{238}U , estimated using the GIF model [6].

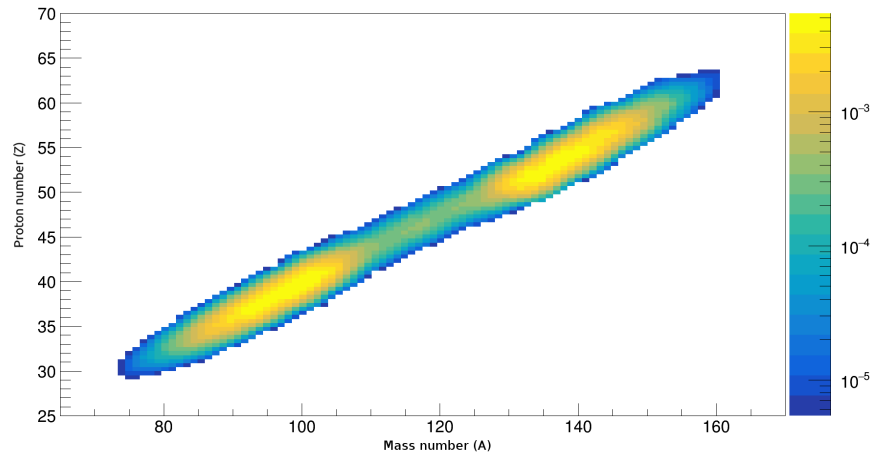


Figure 1.4: Probability distribution, normalized to unity, shown in color (z-axis) for the generation of each isotope in the 14 MeV gamma induced fission of ^{238}U .

The fission process is used by many well established nuclear facilities to produce and make available for measurement more and more exotic isotopes, such as projectile fission at the FAIR/GSI facility in Germany, proton induced fission at the ISOLDE facility at CERN in Switzerland or neutron induced fission at the SPIRAL2 facility of GANIL in France, just to name a few. The other common methods for producing exotic radioactive isotopes are through fragmentation and spallation, processes that take place when a nucleus disintegrates through highly energetic inelastic nuclear reactions with other particles. Future facilities such as ELI-NP will use high energy photons to induce photo-fission in heavy actinide nuclei and thus produce exotic neutron rich isotopes. The details of this method are presented in Chapter 4 of this thesis. The next chapter presents the importance of the neutron rich isotopes for nucleosynthesis and the development of the Universe.

Chapter 2

The role of neutron rich nuclei in cosmology

This chapter describes the link between radioactive ion beam research facilities, the study of the exotic neutron rich nuclei and their impact on understanding the Universe's evolution.

2.1 Cosmology and nucleosynthesis

2.1.1 Birth of the Universe

The Universe represents everything that we conceive thus far. It includes all the matter forming stars, planets, us, and all the forces that fuel its dynamics. It also includes the space and time themselves, presumably strange forms of energy (dark energy) or new types of matter (dark matter) and potentially many other phenomena that we will discover in our journey as a species.

In modern physics, the moment of the Universe's creation is accepted to be the so-called "Big Bang", when space and time began to exist and evolve. No scientific agreed understanding exists for what happened before the creation moment nor how or why this occurred, but science is already doing a great job in understanding many of the things that happened just fractions of a second after the "Big Bang" and all the way to the present day.

2.1.2 The formation of the chemical elements

In the first two to three minutes, the only chemical element created was the hydrogen nucleus consisting of a single proton that gives its atomic number, equal to one in this case and thus listed first in the periodic table of elements. Due to the nuclear force the proton coupled with a neutron to form "heavy hydrogen" called deuteron. The high energy density allowed the fusion of two deuteron nuclei into helium consisting of two protons and two neutrons and thus the second element in the table was created.

Around the age of about 380.000 years the Universe suffered a fundamental change [8] driven by the fact that the energy density was small enough to allow the first photons (rays of light) to travel long distances without colliding with other particles. This is known as the time when the Universe became transparent and the so called "dark age" began, named like this due to the fact that there was yet no star formed to light up the Universe. In parallel massive solid bodies created through the gravitation pull and after a few hundred million years, they developed enough pressure inside their cores to once again allow the fusion of elements to take place, thus synthesizing the next heavier chemical elements all the way up to iron (Fe) and also emitting their characteristic light in the process (star light).

Iron has 26 protons packed together with 30 neutrons thanks to the strong nuclear force and since it is the second most tightly bound known nuclei after nickel (^{62}Ni) it imposes a certain upper threshold for the stellar fusion process. A human body is made up, by mass, of about 65% oxygen (element with eight protons) and 18% carbon (element with six protons) and also about 10% hydrogen (element with 1 proton) generated in the first second after the Big Bang, so we are indeed made of star and primordial material created outside of our planet. Nevertheless, there are heavier elements present on Earth and also in our bodies in small quantities like selenium for example, a nuclei with 34 protons and thus heavier than iron, which it was most probable not created in stars. We use in our technology, elements like zirconium (40 protons), silver (47 protons), gold (79 protons) and so on. Our nuclear power plants are powered by uranium (92 protons) or other very heavy nuclei that could not have been produced in the fusion process taking place in stars. For these heavy elements, other production mechanisms must have taken place, with the most well established theories being presented below.

There are several theories regarding the creation path of the heavy nuclei above iron. The main ones, proposed in 1957 by E.M. Burbidge and A.G.W. Cameron [9] [10], are known as the proton capture process (*p*-process), the slow

neutron capture process (*s*-process), the rapid neutron capture process (*r*-process) and some intermediate processes or specific to certain conditions.

The *p*-process is characterized by proton capture with emission of gamma (p, γ) and is responsible for the production of proton-rich isotopes (*p*-nuclei).

Locations that might have high densities of free protons alongside heavier nuclei with high kinetic energies are likely to be the production sites of *p*-nuclei. High kinetic energy is required to overcome the Coulomb barrier between the positively charged proton and seed nuclei. Core-collapsing supernovae are expected to produce most of the *p*-nuclei due to their strong explosive environments.

The *s*-process is determined by a series of neutron capture reactions that takes place slowly, in time scales of thousands of years. This process takes place along the valley of β -stability which is the area by the (N, Z) combinations of the stable isotopes. The newly created element has a higher mass and if it is unstable, it will decay by transforming the extra neutron into a proton (β^- decay), thus generating the element with the next atomic number. If this process is repeated, elements with higher and higher atomic number are created.

The main production site is considered to be the asymptotic giant branch (AGB) stars, observably red giant stars in an evolved phase of their life, when iron (Fe) is abundant enough. Those are stars that have a mass range between half and eight times the mass of our Sun and have complex layers of different fusion reactions.

The *r*-process is characterized by sequential and rapid neutron captures by seed nuclei, resulting in exotic neutron rich isotopes that will decay via the beta minus channel, similar to the *s*-process but with a greater neutron flux that allows multiple capture reactions before the beta decay, as exemplified in fig. 2.1.

Due to the need of a greater density of available neutrons, potential production sites are searched through the ones that offer such extreme conditions and hot explosive environments like: neutrino-driven winds in supernovae, magnetic-turbulence driven ejecta in magneto-hydrodynamic jets from supernovae and collapsars, accretion disks of neutron stars or black holes, mergers of binary neutron stars or a neutron-star and a black-hole. [11]

The *r*-process mechanism is believed to be responsible for more than half of the nuclei heavier than iron, has great implications in the actual existence and evolution of the Universe and it is invoked many times in the work related to this thesis, thus some important details are presented separately in the next section.

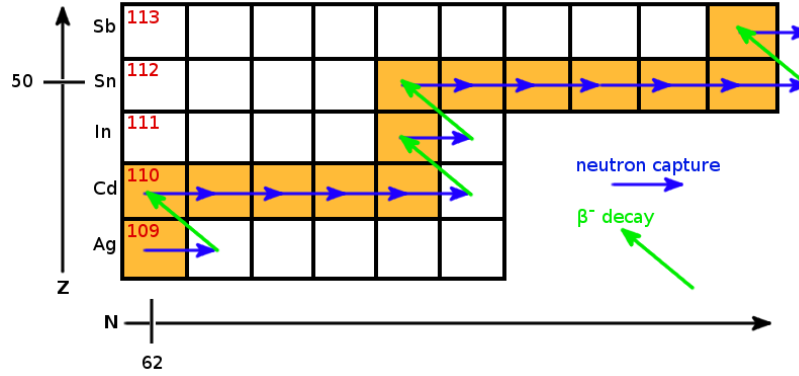


Figure 2.1: Example of r -process pathway (orange) in the Ag-Sb region

2.2 The r -path mechanism in extreme stellar environments

Alongside the nuclear physicists community, astronomers and astrophysicists have also joined the quest for understanding the mysteries of the r -process that, after more than 60 years from when it was first proposed, is still an unsolved puzzle for the creation of heavy elements in the Universe.

One can observe the present abundance of elements in our Solar System environment and to some extent in the visible stars in our Milky Way galaxy or other galaxies. The fraction of heavier elements is called, in astrophysical terms, "metallicity" and there seems to be an universal pattern of r -process element abundances observed, specially for elements in the range of $Z = 50-75$. This leads to the suggestion that a certain recurring combination of events must be involved to produce such pattern [11]. One of the most prominent characteristics of this abundance pattern is related to the $N = 50, 82$ and 126 peaks. Isotopes with closed neutron shells have neutron capture cross-sections that are orders of magnitude lower than the ones with open shells thus the r -process is far less probable in these cases and abundance is peaking [12]. There are still variations of "metallicity" that are usually expressed as a ratio of specific r -process elements as a function of the iron abundance, all measurements being scaled to the ratio of our Solar System. Those differences, especially the most prominent cases, might suggest multiple different r -process environments generated by stellar events of different types, the main ones being briefly presented below.

One commonly studied r -process site is represented by the neutrino winds

generated from core collapse supernovae. In the supernovae core collapsing process, rates of 10^{52} neutrinos and anti-neutrinos are ejected in time scale of seconds [13] generating reactions that transform protons into neutrons $\bar{\nu}_e + p \rightarrow n + e^+$ and neutrons into protons $\nu_e + n \rightarrow p + e^-$. High neutron production capabilities and thus high neutron densities are favored in cases where $\bar{\nu}_e$ are more energetic, or have higher local densities that can create *r*-process elements. That being said, modern simulations [12] suggest, based on the current knowledge of nuclear and neutrino physics, that this mechanism is not the main production site.

Another proposed alternative are the magneto-hydrodynamic jets [14] where matter is ejected due to the high rotational rate in the presence of high magnetic fields leading to neutron rich stars [15] that have the right ingredients to generate high mass *r*-process nuclei.

Binary neutron star systems lose energy by emitting gravitational waves and thus merge at some point through a violent stellar event [16]. This type of events have come into the forefront since the first gravitational waves [17] from the merger of two black-holes were detected via LIGO (Virgo Collaboration) [18]. Black-holes are at this point believed to have little to no impact in the creation of elements in the Universe thus a much more significant observation of gravitational waves is the two neutron stars merging event GW170817 [19]. The follow-up spectral observations of this event showed radioactive decay consistent with the *r*-process elements giving confidence that this type of events, probably alongside neutron-star black-hole mergers, are among the most significant mechanisms of *r*-process element generation [12]. The rate of these events observed throughout the next years could confirm the amount in which these type of mergers are responsible for heavy element creation.

In order to perfect theories and develop models on how the nucleosynthesis takes place one should master many nuclear physics processes such as: neutron capture rates, nuclear masses and structure, β^- decay rates, β^- delayed neutron emission, fission barriers and fission fragment mass and charge distribution as well as neutrino physics which seem to play a great role in the *r*-process mechanism. Attempting to improve knowledge in these topics, the physics community has put a lot of effort in creating facilities that can measure and study the properties of exotic matter such as the *r*-process elements here on Earth.

2.3 RIB facilities as laboratories for exotic nuclei

Due to their important impact on nuclear astrophysics, as discussed in the previous section, but also for the fundamental understanding of nuclear structure, nuclear equation of state, and many more all the way to applied physics, the study of exotic nuclei in the neutron rich region of the nuclide chart remains in the central focus of contemporary nuclear physics.

For this reason, several RIB facilities are currently active worldwide, such as CARIBU (ANL) [20] in USA, ISAC (Triumf) [21], in Canada, ISOLDE (CERN) [22] in Switzerland, FRS (GSI) [23] [24] in Germany, SPIRAL (GANIL) [25] in France, NSCL (MSU) [26] in USA, JYFL (Jyväskylä) [27] in Finland, and RIBF (RIKEN) [28] in Japan. For review see ref. [29]. To a large degree, they complement each other by employing a variety of methods and technologies, such as beam types (from heavy ions to photons), target types (thick or thin), fragment separation (in-flight separators, ISOL and/or in-cell catchers) and selection (with lasers, magnets, time-of-flight spectrometers), as well as experimental stations. Among the RIB facilities with γ -driver beams and thick actinide targets, the current ALTO (IPN Orsay) [30] and the future ARIEL (TRIUMF) [31] facilities employ bremsstrahlung sources, while the future ELISOL facility at ELI-NP will use a (Laser Compton Backscattering) LCB source. When compared to facilities with charged particle or ion driver beams, the facilities with the γ -driver beams have the advantage of negligible background effects due to their primary beam, but also the disadvantage of typically lower RIB production yields.

These impressive developments of RIB facilities have helped measure thousands of isotopes sketched in the Segre chart (fig. 2.2), colored in according to their decay mode. Still, many others, that are predicted to exist have not been measured yet (gray zone in fig. 2.2), mainly due to different technological challenges.

In order to measure and learn the properties of these exotic nuclei one needs to first produce them and this is done through different types of nuclear interactions, as enumerated earlier in this section.

After production, the exotic nuclei are then separated usually with the help of mass separators. These devices make use of their different response of the charge over mass ratio ($\frac{q}{m}$) to electro-magnetic fields. In the same electric field (E), the nuclei with low charge over mass ratio will be less accelerated ($a=\frac{qE}{m}$) than the ones with higher charge over mass ratio, thus allowing separation through the time-of-flight (TOF) method. Similarly, in the same magnetic field (\vec{B}), the

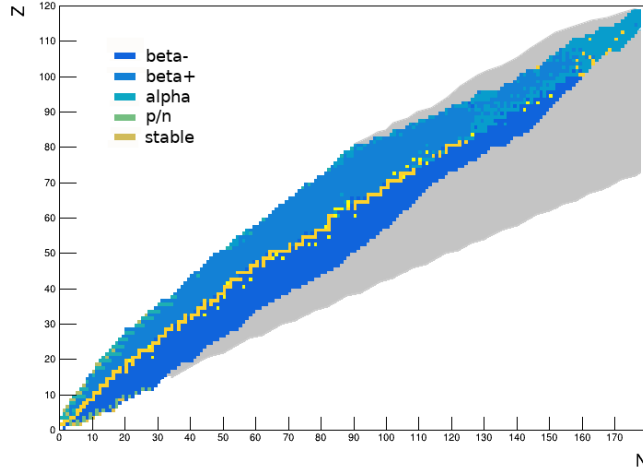


Figure 2.2: Segre chart of isotopes, colors corresponding to different decay modes given in the figure and the gray zone corresponding to experimentally unmeasured nuclei

particles with speed (\vec{v}) will encounter a deflection force $\vec{F} = q(\vec{v} \times \vec{B})$. Because this deflecting force acts like a centripetal force one can write the equation $q(\vec{v} \times \vec{B}) = \frac{m\vec{v}^2}{r}$, where r is the radius of the curvature. Extracting the values of $r = \frac{mv}{qB}$ one can observe that the nuclei with low $\frac{q}{m}$ value will be less deflected (curved) than the ones with high $\frac{q}{m}$ values, thus magnetic fields can also be used for isotope separation.

The well established experimental setup types, built with the goal of generating radioactive ion beams (RIBs) are ISOL and In-flight separators (fig. 2.3).

The ISOL (ion separator on-line) technique [32], sketched in fig. 2.3, uses high intensity beams of light mass particles that impinge on a thick target and produce all types of reactions (spallation, fragmentation, fission, etc) in order to produce radioactive nuclei that are diffusing into an ion source. The target is heated to facilitate the evaporation of the generated nuclei outside it. The resulting RIB has good quality allowing detailed studies of nuclear reactions and structures with stopped-beam experiments such as the ones involving ion traps and laser spectroscopy. Possibly, the most prominent characteristic of this method is that due to the fact that high intensity driver beams are available, in combination with thick targets, the resulting yields of radioactive ions are large. Still, there are two main disadvantages: firstly, the extraction is strongly dependent on the chemical properties of the produced isotopes, thus the most chemically active ones are hard

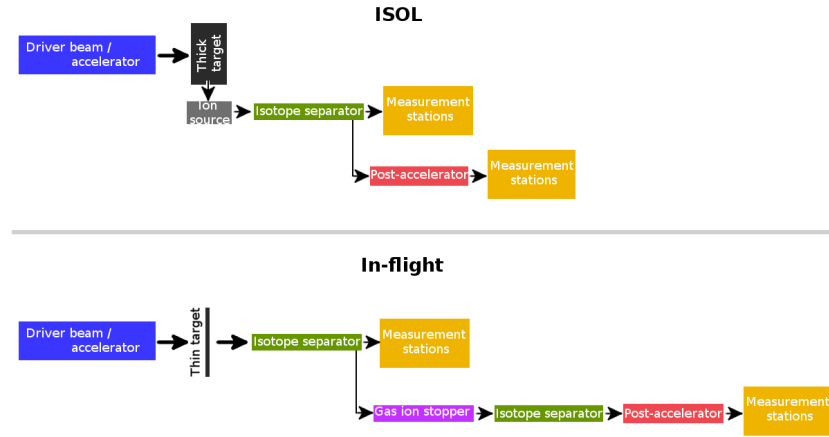


Figure 2.3: Diagram showing main features of the ISOL and in-flight techniques

to transport outside of the thick target, particularly the refractory elements which are not available in this method because they do not evaporate due to their high melting point; secondly, the short lived products are not available due to the long time required for diffusing outside the target.

The in-flight technique [33], sketched in fig. 2.3, uses high intensity beams of heavy mass particles that collide with thin targets producing mainly fragmentation. The resulting radioactive nuclei conserve their high momentum in the forward direction of the beam and thus they can be quickly mass separated in-flight, making available measurements for short-lived isotopes before they decay. This method also solves the problem of the chemical dependence of elements due to the kinematic extraction of the resulting nuclei. Still, one of the main drawbacks is that the resulting radioactive beam has a large spread in energy and angle thus the experiments that require bunches or stopped beams are not suitable.

During my PhD, I was involved in many experimental campaigns for mass measurements at the Ion catcher setup - Fragment Separator (FRS) of the GSI facility in Darmstadt, Germany (resulting paper in reference [34]); multi-nucleon transfer reaction measurements at University of Jyväskylä (JYFL), Finland (resulting paper in reference [35]), collinear laser spectroscopy at the ALTO facility in Orsay, France (resulting paper in reference [36]) and other charged particle and gamma spectroscopy experiments (resulting papers in reference [37], [38], [39]). I have also been involved in the data analysis of the results of such experiments as well as preparatory simulations and calculations that I will present in the next chapters of the thesis (resulting papers in reference [40], [41], [42]).

Chapter 3

Prompt fission γ -rays in $^{233}\text{U}(\text{n}_{th},\text{f})$

This chapter presents an original work consisting in data analysis of the γ -rays that were recorded during a $^{233}\text{U}(\text{n}_{th},\text{f})$ experiment described below. The data processing, calibration and sorting methods are presented leading to the determination of the prompt fission γ -rays spectrum. The measured spectrum is unfolded of the detector response function towards extracting energy and multiplicity properties of the emitted prompt fission γ -rays. The unfolding was done using the matrix inversion method [43] and included the construction of a detector model and the performing of extensive simulations in order to describe the detector response.

3.1 Experimental setup at Budapest Nuclear Reactor

This experiment was performed at the Hungarian Academy of Sciences Center for Energy Research (MTA EK) in Budapest. This facility runs a light water nuclear reactor of low power, used for scientific studies, that can provide a thermal neutron beam with a flux of $5 \cdot 10^7 \text{cm}^{-2}\text{s}^{-1}$.

The fissile material used is ^{233}U in the form of 2 UO_2 samples: one of mass 1818 μg , thickness 144 $\mu\text{g}/\text{cm}^2$ and diameter of 40 mm and the second of mass 2010 μg , thickness 160 $\mu\text{g}/\text{cm}^2$ and diameter of 40 mm. The targets were mounted on Al-backings (25 μm thickness and 40 mm diameter). The estimated fission rate for both targets is $2.6 \cdot 10^5 \text{s}^{-1}$.

The goal of this experiment was to test and develop the data acquisition system at ELI-NP, to prepare the data analysis methods while measuring Prompt Fission Gamma Ray Spectra (PFGS). The analysis of PFGS also has impact on improving

the fundamental understanding of the fission decay channel and present interest for the design restrains of future nuclear reactors.

The two uranium samples were placed back to back inside a special interaction chamber that had a central cathode and two side anodes and was equipped with grids, on both sides, used for detecting the fission fragments thus providing trigger signal for the data acquisition.

Four scintillation detectors were used, three LaBr₃:Ce (2 inch × 2 inch) placed at 30 cm from the interaction point and one LaBr₃:Ce (3 inch × 3 inch) placed at 40 cm from the interaction point.

Two data acquisition systems (DAQs) were used: one was made available by JRC Geel and a second digital system, from ELI-NP, that used MIDAS acquisition framework.

3.2 Data analysis

3.2.1 Energy calibration and energy resolution

Energy spectra have been recorded using several radiation sources such as ⁶⁰Co, ¹⁵²Eu, ²⁰⁷Bi and from a special organic compound called "UreaD" (ND₂COND₂) [44] that emits high energy gamma rays up to 10 MeV when bombarded with neutrons. Also data with no beam and without radioactive sources was also recorded for further background assessment and subtraction.

For the higher energy range, a linear plus exponential fit was used for describing the channel to energy calibration function, as shown in fig. 3.1.

The relative energy resolution in the form of ($\frac{\Delta E}{E}$), where ΔE is the full width at half maximum (FWHM) has been computed, using the ¹⁵²Eu source data, and plotted as a function of the mean energy of the corresponding peak (E) and then fitted with a power function $\frac{\Delta E}{E} = a \cdot E^b$ as shown in fig.3.1.

3.2.2 Unfolding the recorded data from the detector response function using the matrix inversion method

In a common experiment, one needs to be able to detect (measure) the result (what comes out of that particular experiment). In present day nuclear physics experiments one relies on specialized electronic devices in order to detect the outcome (usually different types of radiation) however records what the equipment is observing which is not always equal to the radiation generated in the experiment

spectra as multiple Compton scattering interactions, pair production processes, appearance of special effects like escape peaks, backscattering peak, pile-up and so on.

One method that takes all these effects into account and offers a way to better assess the real emitted spectrum by unfolding the measured data from the detector response function is called the matrix inversion method.

The matrix inversion method is based on the idea that one can model and simulate the whole detector response for every gamma ray energy bin present in the spectrum of interest. In this way one obtains the detector response to each energy of the incident photon. If done correctly one approaches the mathematical probabilities that a gamma ray of a certain energy can be measured as being of other energies in the established range.

3.2.3 GEANT4 simulations for assessing the detector response

The complex detector response is not generated just by intrinsic detection mechanisms but is also a function of its environment due to different particle scattering probabilities from the surrounding objects, thus the task is then to model not just the detecting system but the full experimental setup in order to obtain the correct detector response. In this case the GEANT4 framework has been used to simulate the physics of the entire experiment setup, shown in fig. 3.2 and finally generate the detector response matrix.

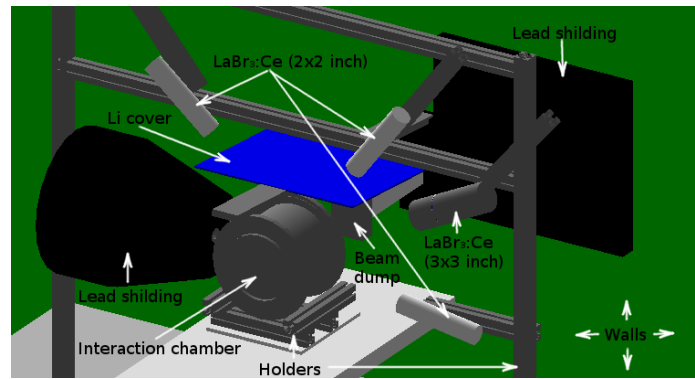


Figure 3.2: Experimental setup geometry overview constructed in GEANT4. Main elements are labeled in the figure.

A special function has been built and used to collect the energy that the radiation deposited in the crystal volume and sum it up for all the interaction steps in

one event. Many mono-energetic events were simulated and results were stored in an energy histogram thus simulating the detector response for a particular incident energy. This has been then repeated for all the incident energies corresponding to all the energy bins up to 10 MeV.

For validation purpose the ^{60}Co has been simulated (shown in Fig. 3.3).

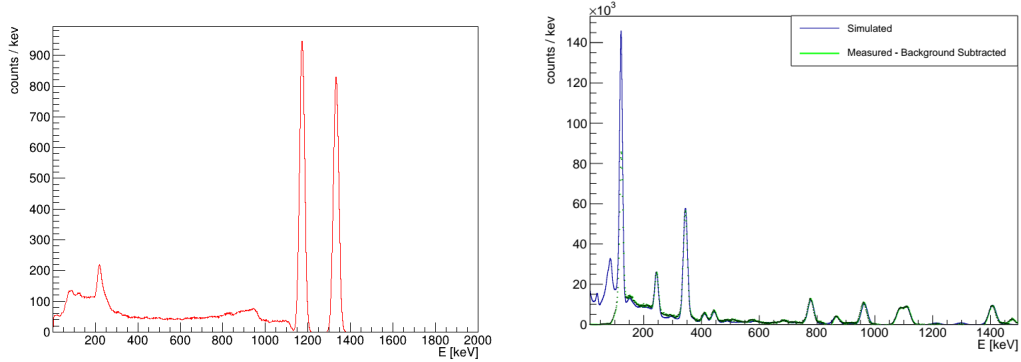


Figure 3.3: ^{60}Co simulated spectrum (left frame). ^{152}Eu simulated spectrum folded with the observed energy resolution of the detector (blue) compared with the ^{152}Eu measured and background subtracted spectrum (green) (right frame)

One can observe the two specific mono-energetic transition gammas but, as expected, additional features appeared due to Compton scattering of the photons, the backscattering phenomenon and so on.

After the simulation of a more complex source (^{152}Eu), the agreement between the simulation result and measured data was verified as shown in fig. 3.3. One of the most prominent difference appears in the lower energy part of the spectrum, where the measured data are cut at about 100 keV most probably due to the detector set threshold.

In our case study, a variable binning was performed using half of the observed energy resolution of the detector as a bin size (calculated for each energy bin) just to ensure that information is preserved.

The scintillator detectors pulses were recorded using a fission trigger provided by the interaction chamber as described in the experimental setup section of this chapter. Using the time stamp of the fission trigger signals as start moment and the scintillator recorded time stamp as the stop point, the distribution of the γ -rays flight time could be reconstructed.

The measured γ -rays time of flight (ToF) has been plotted against their energies in fig.3.4 giving an overall view of the different signal contributions and pro-

viding means to filter the prompt fission γ -rays. In this study, the prompt time window was determined to be $\Gamma = 5.6$ ns, parameter extracted from fitting the ToF distribution (right side of fig.3.4) with the Lorentzian function $L(x) = \frac{1}{\pi} \frac{\frac{1}{2}\Gamma}{(x-x_0)^2 + (\frac{1}{2}\Gamma)^2}$ where Γ is the distribution width and x_0 its center. This function was found to describe best the distribution in this case.

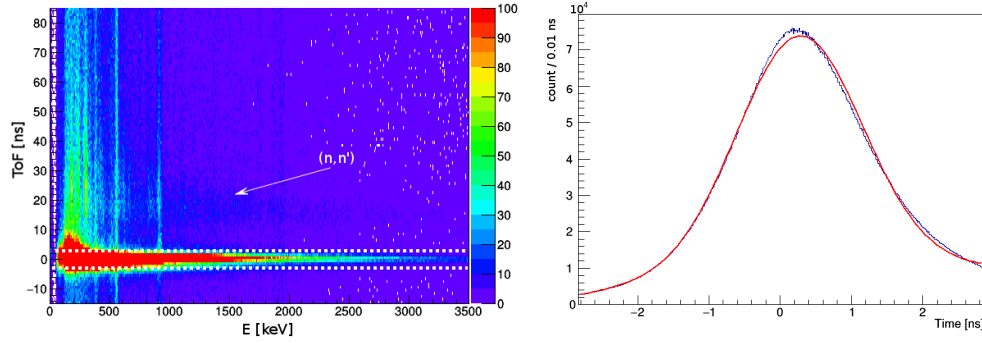


Figure 3.4: Measured γ -rays time of flight against their energies (left) and the projection on the time axis (right). White dashed lines illustrates the prompt fission γ -rays window.

The main features that emerge in this representation are the prompt fission γ -rays, the broad delayed signals that are generated by γ -ray emission due to the prompt neutron elastic scattering (n,n') reactions, some background signals that are constant in time but also some mono-energetic delayed γ -ray emissions probably coming from isomeric excited states of the fission fragments.

After the prompt fission γ -ray determination and the unfolding of the detector response, characteristics of the emitted prompt γ -rays could be extracted, such as the average energy \mathcal{E}_γ .

3.2.4 Response matrix calculations

Applying the method described above, the full response matrix, shown in fig. 3.5, has been generated with an energy range starting from 50 keV, all the way up to 10 MeV. In the referred figure one can observe, parallel to the x axis, the yields composing the simulated energy spectra of an incident gamma ray of a single energy with value corresponding to its bin on the y axis.

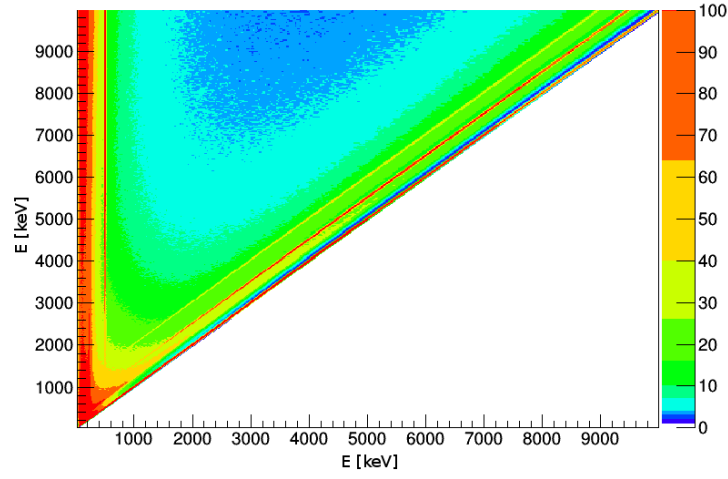


Figure 3.5: Detector response matrix up to 10 MeV.

Due to the same binning being used for all the spectra involved in the method, including the simulated ones, the generated response matrix is mathematically a square matrix, thus it can be inverted. The inverse is then applied on the prompt fission gamma rays measured spectrum to unfold it from the detector response and obtain the emitted spectrum shown in fig. 3.6.

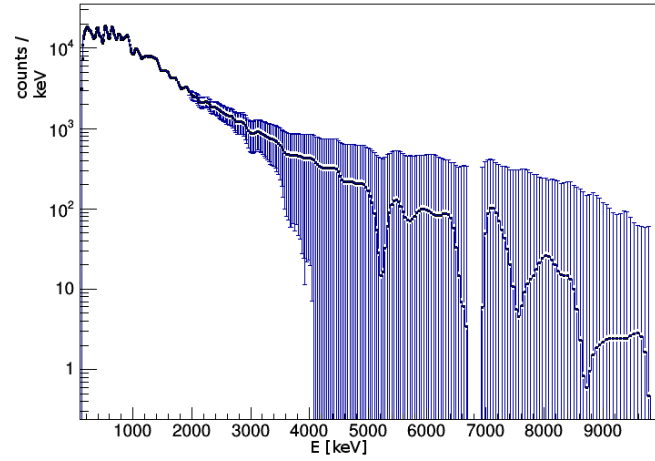


Figure 3.6: Prompt fission γ -rays spectrum unfolded from the detector response.

One effect of the matrix inversion unfolding method is that the unfolded spectrum has big statistical fluctuations due to the high correlation between neighboring bins and the choosing of the optimum regularization or smoothing strength for the resulting spectrum could be challenging. There are many regularization techniques, in this case the Tikhonov [45] method was chosen that is implemented in newly developed smoothing software solutions as TUnfold [46] or RooUnfold [47] classes available in ROOT framework [48] and as open source.

The smoothing applied to the resulting data is based on the 353HQ algorithm [49] that has a multi-step procedure, first taking the median of three neighboring bins, then the median for five and again for three neighboring bins, the main assumption being that the true spectrum is reasonably continuous for small intervals.

Based on the regularized prompt fission gamma ray spectrum, average prompt gamma ray energy was calculated to be $\epsilon_\gamma = 854.39 \pm 3.03$ keV result that is close to previous publications that provide $\epsilon_\gamma = 840(2)$ keV for a similar but not identical fissioning system $^{235}\text{U}(n_{th},f)$ [7]. The result demonstrates that the procedure is reliable and can be used and further developed for unfolding the measured spectra from the detector response and obtaining the true emitted spectra needed in the data analysis of most experiments.

Chapter 4

Photo-fission mechanism for RIB generation

In this chapter, it is presented the original work of optimizing the ion yields of the ELISOL radioactive beam facility proposed at ELI-NP. Various nonindependent parameters are taken into account such as: target system geometry, target thickness and tilting angle and beam energy. Optimized parameters are found through GEANT4 simulations and in conclusion the optimized total ion yield is presented along the main strong points of this special design experimental setup. This chapter is based on the publication "Optimization of photo-fission fragment production in the ELISOL setup at ELI-NP", *U.P.B. Sci. Bull. A*, 82, 2020, in which the thesis author is the writer and first-author of the published paper.

4.1 RIB generation driven by CBS gamma beams

A new major nuclear physics research infrastructure currently under construction in Europe is Extreme Light Infrastructure Nuclear-Physics (ELI-NP) [50]. The status of the implementation of ELI-NP and the emerging research program were reviewed recently [51]. Its main research instruments will be two 10 PW laser beams [52], and a high-brilliance gamma beam that will be produced through Compton Back Scattering of laser photons off highly energetic electrons accelerated with a linear particle accelerator [53].

This work extends the study presented in Ref. [54] by using the actual target design and an improved parametrization of the photo-fission data. In addition, the experimental setup is optimized, taking into account several factors such as

target thickness, number, geometry and tilting angle, as well as the gamma beam energy window in order to maximize the rate of fission fragments released in the gas of the CSC and minimize the rate of fragments that are stopped in the targets, backings, frames or in the rods supporting the target system.

4.1.1 The ELISOL beamline at ELI-NP

An Isotope Separator On-Line facility is proposed at the ELI-NP (ELISOL) for the study of neutron rich nuclei [55] [56]. It uses the photo-fission reaction induced by exposing uranium targets to the high-brilliance $10^{12}\gamma/s$ gamma beam at ELI-NP in the energy range 10 MeV-19 MeV. The targets are placed in the center of the High Areal Density with Orthogonal extraction Cryogenic Stopping Cell (HADO-CSC), a concept introduced in Ref. [57]. The HADO-CSC consists of two chambers: production chamber and extraction chamber (Fig.4.1). To form a radioactive ion beam (RIB) from the fission fragments released with high kinetic energy, they need to be slowed down and extracted. To achieve this, the CSC is filled with low temperature He gas and the target system is placed inside it. The ions of the fission fragments will be slowed down in the gas and guided with both electric fields and gas flow to the extraction chamber. To avoid the loss of ions by hitting the cell walls, RF fields will be used. The RF Carpet will generate a strong repulsive electric field perpendicular to the wall. Fig. 4.1 shows the stages of fragment production, release and extraction. Downstream from the CSC, a Radio-Frequency Quadrupole (RFQ) will form the RIB to be sent to the measurement stations.

4.1.2 Improved photo-fission model

The extended parameterization GIF^{238U} [6] of all available measurements of uranium photo-fission cross-sections and production yields has been implemented in the GEANT4 [58] modules described in Ref. [56]. This model covers a broad gamma energy interval from 0 to 30 MeV and reliably extends the description of the mass and charge yields into the heavy fragment region.

This improved parameterization was used to cross-check previous simulations [54] [56] which were based only on the photo-fission yield measurements in ultra-peripheral $^{238}\text{U}(\gamma^*, f)^{208}\text{Pb}$ collisions [59]. Experimental data are available for $Z \leq 52$, and an extrapolation was done for higher proton number. More recent measurements [60] extend these data and, as described in Ref. [6], a strong deviation from a monotonic behavior develops in the heavy fragment region after

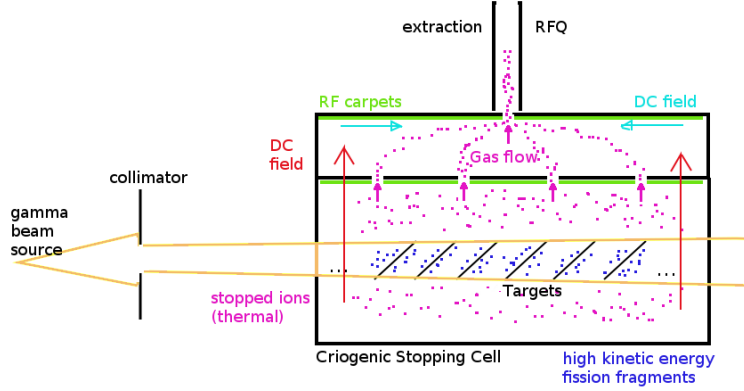


Figure 4.1: The motion of photo-fission fragments in the Cryogenic Stopping Cell (pink). The gamma beam (orange) is hitting the uranium compound targets (black) inside the CSC producing high kinetic energy photo-fission fragments (blue). The fragments are slowed down in the gas inside the lower chamber of the CSC becoming thermalized ions (pink) which are guided to the upper chamber using the vertical DC field (red) and the gas that flows upwards through the 4 nozzles. RF carpets (green) are used to repel the ions from the upper walls of the chambers. In the upper chamber a combination of horizontal DC fields (cyan), upward gas flow and RF fields (green) will help extract the ions.

the cut off of the data set of Ref. [59]. Two GEANT4 classes were upgraded using the above parameterization, namely the classes for calculation of the total photo-fission cross-section and for the generation of the final state products.

4.1.3 Design and optimization of the target system

Previous work [54] [56] considered metallic uranium as target material. However, practical considerations related to mechanical and chemical properties of the targets, brought in consideration the use of various uranium compounds, such as uranium oxide UO_2 , uranium carbide UC_2 and uranium tetra-fluoride UF_4 .

GEANT4 simulations have been performed for the three mentioned compounds and compared with the metallic uranium for different target thicknesses. The result of these calculations are presented in Fig. 4.2. An optimal areal density of 3 mg/cm^2 is obtained for all target materials.

In the present study we used uranium tetra-fluoride targets with a $3 \mu\text{m}$ optimal thickness embedded in 5 mm thick AlMg_3 target frames held together by four Fe

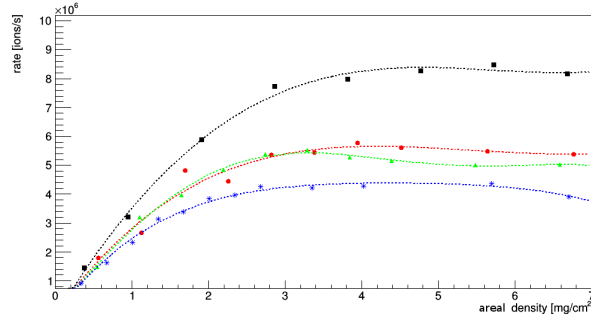


Figure 4.2: Yield of the released fragments as a function of the area density for the 3 uranium compounds UF_4 (blue stars), UC_2 (red circles), UO_2 (green triangles) and metallic uranium (black squares).

rods, 3 mm in diameter. The targets have a $0.5 \mu\text{m}$ graphite backing.

The release rates, shown in Fig. 4.2, are obtained using a target system composed of 59 targets tilted at 10 degrees. At these rates the ion fraction stopped in all the target frames (about 15%), in the four rods (about 4%) and in all the neighboring targets and graphite backings (less than 3%), were included.

In the full CSC device of ELISOL, a large number of targets will be placed along the primary gamma beam. As described in Ref. [54], the geometry of this target system has several parameters that establish how the gamma beam spot is covered and how the available space inside the CSC is used optimally. We revisit here the optimization study, described in Ref. [54], and take in consideration the actual target and target frame design.

Circular targets, tilted with respect to the gamma beam, are seen as elliptical by the beam. Hence, they cannot cover the cylindrically symmetric spot. Therefore, sets of two or three targets placed one on top of the other have been considered creating target sets to better cover the primary beam spot.

A complex optimization study of the target system geometry was performed in order to maximize the release rate of photo-fission fragments into the CSC gas. The main parameters of the optimization, and a description of their impact, are:

- (1). The maximum energy of the gamma beam E_γ^{max} which is fixed by the energy of the accelerated electrons, as described in Ref. [54]. This sets the overlap between the beam intensity distribution and the photo-fission cross-section, as exemplified in Fig. 4.3. The gamma beam energy distribution is cut on the left side by the collimator due to the angle-energy correlation of the Compton back-

scattering. The values used in the calculation are for $E_{\gamma}^{max} = 14, 14.5, 15, 16$ and 17 MeV.

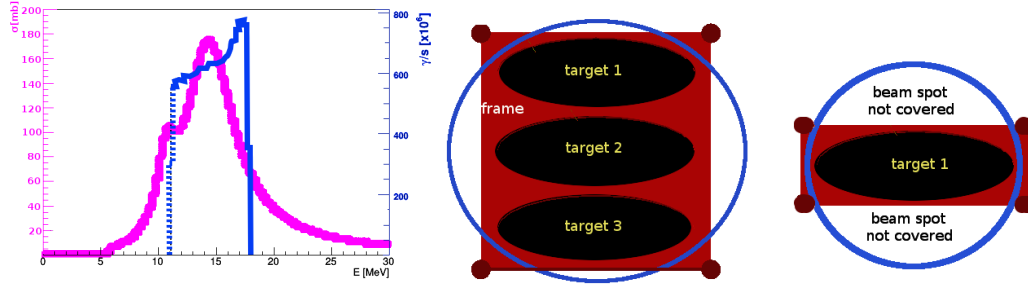


Figure 4.3: Gamma beam intensity distribution (blue line) overlapped with the photo-fission cross-section (pink line) (left). Difference in the beam spot size (blue circle) coverage ratio between three targets per set and one target per set (right).

(2). The target tilting angle with respect to the primary beam. Smaller values of the tilting angle increase the path length of the gammas inside the target foils, hence the fragment production rate, and also increase the available emission angle relative to the neighboring foils.

However, decreasing the tilting angle increases the longitudinal size of the target set and reduces the overall number of sets that can be placed inside the CSC. The values used in the calculations are tilted angles of 10 and 20 degrees.

(3). The number of targets per set which establish the coverage of the beam spot size. The largest dimension of the target on the orthogonal plane with respect to the beam axis fixes the beam spot size. However, due to the small tilting angle one dimension of the target is covering only a small fraction of the beam spot. Therefore, the increase of the number of targets per set gives a better coverage. This is demonstrated by the drawing in Fig. 4.3. The values used for calculations are one, two and three targets per set.

(4). The number of target sets which has impact on production rates. A larger number of targets is desired, however it is limited by the total length of the target system which was set to 2 m in these simulations.

4.1.4 Estimated RIB production yields

A large number of configurations have been simulated. In the simulations, in order to minimize the computational requirements, a number of 10^8 gamma rays

has been generated for each configuration.

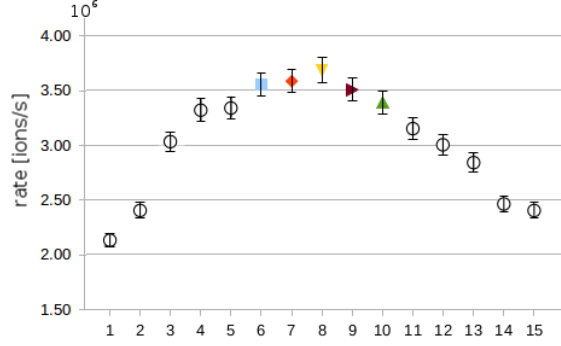


Figure 4.4: The five target system configurations with the highest ion release rate (with colored symbols) and the non-optimal configurations (open gray circles). Each result shown corresponds to a specific system configuration. These configurations are numbered from 1 to 15. Three of the configurations have the value of the gamma beam threshold energy $E_{\gamma}^{max} = 14.5$ MeV: light blue for the results of 1 target/set tilted at 10 degrees, light red for the results of 2 targets/set tilted at 10 degrees, yellow for the results of 2 targets/set tilted at 20 degrees. The green triangle corresponds to the results of 3 targets/set tilted at 10 degrees configuration with $E_{\gamma}^{max} = 15$ MeV. The dark red marker corresponds to the results of 3 targets/set tilted at 20 degrees configuration with $E_{\gamma}^{max} = 16$ MeV.

Those with the highest fragment release rates, within 2σ uncertainty, were selected for runs with increased statistics, more specifically with $4 \cdot 10^8$ gamma rays. The final five configurations are shown in Fig.4.4 and give an estimated maximum rate of released and thermalized fragments of $3.5 \cdot 10^6$ ions/s, corresponding to the expected gamma beam rate of 10^{12} γ /s. The decision on which of these to be implemented will be made based upon criteria related to manufacturing and installation.

This original work and discussions are presented in the publication authored by D. Nichita et al, "Optimization of photo-fission fragment production in the ELISOL setup at ELI-NP", *U.P.B. Sci. Bull. A*, 82, 2020.

Chapter 5

Radioactive ion beam production at the Gamma Factory

This chapter presents an original work that proposes a radioactive ion beam facility at the Gamma Factory [61] at CERN. This proposal is based on the high areal density orthogonal extraction cryogenic stopping cell (HADO-CSC) design optimized in the previous chapter having the Gamma Factory γ beam as driver. This proposal demonstrates competitive yields in comparison with well established facilities while making available many new masses in the far neutron-rich part of the isotopic chains specially in the Zr-Mo region with $A \approx 100$ and in the heavy rare-earth region around Ce $A \approx 140$ as well as for the case of refractory elements. Physics cases opportunities are also presented that link different potential new measurements, made available by the proposed setup, with implications in astrophysics cases and nuclear structure understanding and modeling. This chapter is based on the publication "Radioactive ion beam production at the Gamma Factory", *Ann. Phys. (Berlin)*, 2100207, 2021 in which the thesis author is the writer and first-author of the published paper and also on the "Physics opportunities with the Gamma Factory", paper in preparation by the author.

5.1 The Gamma Factory facility at CERN

5.1.1 Project description

The Gamma Factory (GF) [61] is currently a project at the Conseil Européen pour la Recherche Nucléaire (CERN) located near Geneva, Switzerland. Gamma Factory

facility at CERN can provide the next generation γ beams, based on resonant absorption and emission of laser photons on partially stripped ultra-relativistic heavy-ion (PSI) beams. The laser beam is tuned for exciting a specific atomic transition on the PSI thus emitted characteristic x-ray photons on decay. The x-rays are transformed in high energy photons due to the Lorentz boost given by the ultra-relativistic ions traveling in the accelerator system.

The state-of-the art γ -beam facilities, such as HI γ S at Duke University, USA [62] or the VEGA system at ELI-NP, which is in a final stage of construction at Magurele, Romania, are based on Compton back-scattering of laser photons off relativistic electrons (LCB). The γ -beam flux at the GF is expected to be several orders of magnitude higher compared to the present generation γ -beam facilities. This is mainly due to the interaction cross section which is higher by up to nine orders of magnitude for the absorption of laser photons by PSIs than that for LCB.

5.1.2 Beam generation and properties

Photon emission in the helium-like calcium PSI beam collisions with the laser pulses at the GF facility has been simulated with the Monte Carlo event generator GF-CAIN [63, 64]. GF-CAIN is a version, adapted for the Gamma Factory, of the simulation code CAIN [65] developed at KEK (Japan) for beam-beam interactions at the International Linear Collider (ILC). The interactions between laser photons and PSI beams in GF-CAIN include an atomic absorption of laser photons by a helium-like Ca ion and its subsequent de-excitation by spontaneous or stimulated emissions, including a finite lifetime of the ion in the excited state. In the laboratory reference frame, this lifetime (~ 14 ps) is shorter than the laser pulse duration (50 or 500ps), hence a single Ca ion can be excited many times during the bunch-crossing, and as a result can emit multiple photons. On average, the number of emitted photons per ion is in the range 5.5–38.6 for the laser pulse duration between 50 and 500ps with the pulse energy between 0.5 and 2.0mJ.

The settings detailed were chosen to obtain a γ beam with a maximum energy of $E_{\gamma}^{max} = 18.7$ MeV, which covers the photo-fission Giant Dipole Resonance (GDR) of usual actinide targets, like $^{238}_{92}\text{U}$ or $^{232}_{90}\text{Th}$ [66]. The energy-angle correlation for the γ -rays emitted by the GF source with these parameters is shown in fig.5.1. The tuning of the GF parameters and the GF-CAIN simulations were done by W. Placzek, member of the GF collaboration.

Together with the possibility to set the minimum energy by collimation, this leads to an important property of a PSI-driven γ beam, namely that its energy

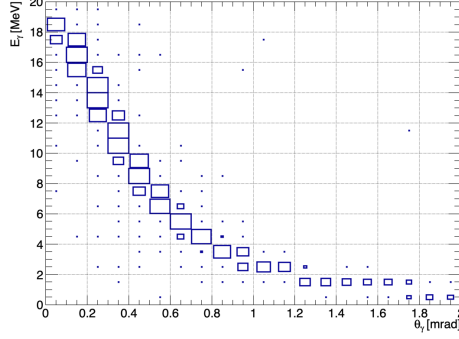


Figure 5.1: Energy–angle correlation for γ emission by $^{40}_{20}\text{Ca}^{18+}$ PSI beam at 89.4 TeV.

range is tunable. For example, the GDR range of approximately 10–18 MeV is covered by collimation of the γ beam to $\theta_{\max} \approx 0.4$ mrad and by tuning the γ_L and E_l beam properties. LCB-driven gamma beams have the same energy–angle correlation, with the notable difference that a given E_{γ}^{\max} is reached at much lower electron-beam energy due to the low mass of the electron. Another common feature of these two γ -beam generation processes is the very narrow angular divergence $\sigma \sim 1/\gamma_L$, which allows for very high fluxes on photo-fission targets. The bremsstrahlung-driven γ beams have significantly weaker energy–angle correlations and much broader angular divergences, making them suitable as primary beams for RIBs, only when placed very close to the targets.

5.1.3 RIB formation with ion catcher

One of the potential applications of this unprecedented γ -beam intensity is the generation of high yield radioactive-ion beams (RIBs) via photon induced fission. The fission process has been used successfully in the production of intermediate mass ($A \sim 70–150$) nuclides in the neutron-rich region far away from the valley of β stability. The study of exotic nuclides in this region is the test-bench for theory in areas like the nuclear equation of state, nuclear structure models and nucleosynthesis via the rapid neutron capture process (r -process). Recent measurements of γ -radiation spectra emitted from neutron star mergers [67] have indicated that these cosmic events are one of the likely locations where r -process nucleosynthesis takes place. This has increased the interest in studying the neutron-rich nuclides along the r -process path, with special interest around the waiting points

at neutron numbers $N = 50$, $N = 82$ and $N = 126$, the first two being accessible in fission, while the last is reached in fragmentation or multi-nucleon transfer reactions.

As it will be argued in this study, a GF-based RIB facility has high production yields, while keeping background effects generated by the primary beam, like the space charge effect, at a very low level.

The GF gamma beam, tuned to cover the GDR photo-fission energy range, is used to irradiate an actinide target, like ^{238}U or ^{232}Th . In order to generate a significant fission rate and due to the relatively low integrated photo-fission cross section $\sigma_{\gamma f}(^{238}\text{U}) \approx 1 \text{ b} \cdot \text{MeV}$ [66], this target needs to be thick (a couple of centimeters). Fission fragments are released from thick targets in ISOL-type facilities by evaporation after heating them to around 2000°C . Examples of the ISOL facilities are ISOLDE [22], which induces fission with a proton beam, and ALTO [30], which induces fission with a bremsstrahlung γ beam. Although the ISOL method generates high fission rates, it has two shortcomings. The first one is that a large fraction of fission products are refractory elements, with evaporation temperatures in the $3500\text{--}4500^\circ\text{C}$ range, and are not released from thick targets. The second is that thermal diffusion is a relatively slow process and, in the constant push to populate RIBs with ever more exotic short-lived nuclides, it has become difficult to use.

As shown in chapter 3 of this thesis, the solution is to split the thick target in many thin (a few microns) targets. Fission fragments are then released kinematically, due to their large initial kinetic energy of $50\text{--}120\text{MeV}$. The fragment release is now element-independent and practically instantaneous. Since their release energy is still significant, they need to be slowed down in a gas enclosing the targets which fills the reaction chamber, called 'gas-cell'. After thermalization, the fragments are extracted from the cell by the gas flow through a narrow exit nozzle where a supersonic gas jet is formed. This is the IGISOL production method, first used at JYFL [27] and broadly used at many RIB facilities. The remaining drawbacks of this method is the large extraction time $\sim 100\text{--}200\text{ms}$ and small extraction efficiency $< 1\%$ of heavy ion transport with gas flow. This is especially true for large gas cells such as the one needed in the case studied here.

The last step in designing an appropriate gas cell is to extract the heavy ions produced in photo-fission with electric fields, rather than with gas flow, drastically improving the transport time and efficiency. This involves a volume DC field that drifts the heavy ions in thermal motion throughout the gas towards the wall with the exit nozzle. A surface RF field on that wall is also needed to catch and transport them towards the nozzle. Therefore, specialized electric devices, called

radio frequency carpets (RFCs) [68], are placed on the cell exit wall.

The ion catchers using electric fields have two potential issues to overcome. The first is the neutralization of the thermalized heavy ions by electron capture. This does not happen with the He gas, which is typically used in ion catchers, due to its high ionization potential. Molecules of gas impurities can, however, easily release electrons to the heavy ions with which they collide. Therefore, the inert stopping gas has to be kept at a very high-purity level of around 1 ppb. The second issue is the ionization of the He gas by the energetic heavy ions during their slowdown, leading to the formation of a He_3^+ ionic cloud. When it becomes strong enough, this space-charge plasma effect can completely overcome the electric fields created by the electrodes and stop the heavy ion extraction. The space charge effects for the extraction of RIBs in the particular case discussed in this chapter will be analyzed in the next section.

The particular ion catcher technology proposed for the RIBs production at the GF facility is the high areal density with the orthogonal extraction cryogenic stopping cell (HADO-CSC) introduced in Reference [57]. This device is developed in collaboration by GSI (Germany), the Giessen University (Germany), ELI-NP (Romania), Soreq (Israel) and JYFL (Finland) for the future RIB facilities at FAIR/LEB, ELISOL (ELI-NP) and SARAF (Soreq). The HADO-CSC introduces several technological improvements over the state-of-the-art ion catchers. The gas purity is kept at about 1 ppb by continuously recirculating and purifying the He gas with a system of active and passive purifiers and also by cooling the inner chambers to the temperature around 75 K, which freezes most of the impurities on the walls. The heavy-ion drift orthogonal to the primary beam, as opposed to the standard longitudinal drift, allows for much higher DC fields without increasing the voltages applied on the electrodes. Due to the high fields, the HADO-CSC can operate at space charge rates with five orders of magnitude higher than the current design. There are several other important improvements of this design described in detail in Reference [57].

5.1.4 Simulation of production rates

For estimating the production rates of an ELISOL-type [54] RIB facility at the GF, we have performed GEANT4 [58] simulations using the beam parameters (the energy–angle correlation, the energy distribution and intensity) and the relevant parts of the ELISOL setup, shown in fig.5.2, consisting of a HADO-CSC with dimensions of 25 cm×25 cm in orthogonal plane and about 2 m in lengths filled with pure He at 300 mbar and 75 K hosting 54, UO_2 , 3 μm thin circular targets

inclined at 10° with respect to the beam axis, parameters that were found optimal for the photon-induced RIB creation in the previous study [40].

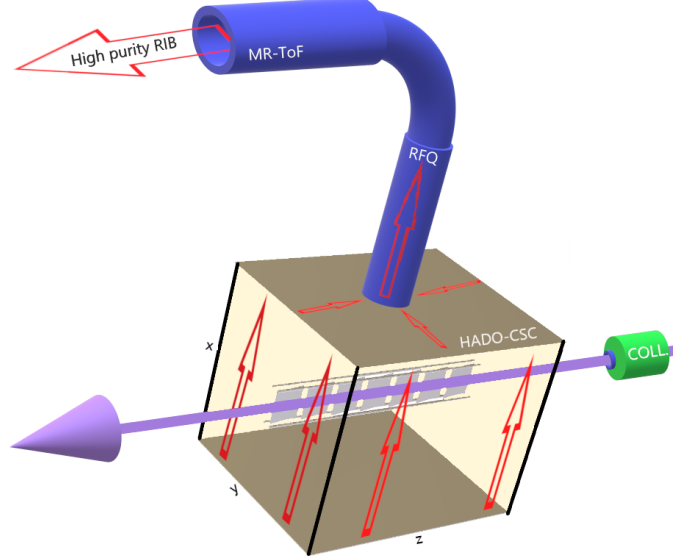


Figure 5.2: ELISOL generic setup scheme depicting the γ beam (purple) hitting many thin targets (light gray) placed inside the He filled HADO-CSC. The produced fission fragments are extracted using electric fields (red arrows), formed into a beam by a radio-frequency quadrupole (RFQ) and finally obtain a high-purity RIB using a multi-reflection time of flight (MR-ToF) mass spectrometer.

The proposed distance of the target system with respect to the GF interaction point is 100 m with the corresponding beam profile shown in fig.5.3. The beam is collimated such that it completely covers the first target of the setup, thus eliminating the unnecessary γ -rays that produce just background. The long distance from γ beam interaction point to the target system is needed for getting outside the ion beam path, due to the small curvature of the accelerator.

The targets projection in the plane orthogonal to the beam is depicted by the black ellipse in fig.5.3. After collimation, the beam fraction hitting the target system at that particular distance is about 3% of total intensity, about 6×10^{15} gammas/second in absolute numbers.

Using the GIF model [6] for photon-induced fission and GEANT4 framework, we estimate the yield, mass and charge distribution and the energy of the produced ions. We track the ions escaping the targets and are released in the gas and com-

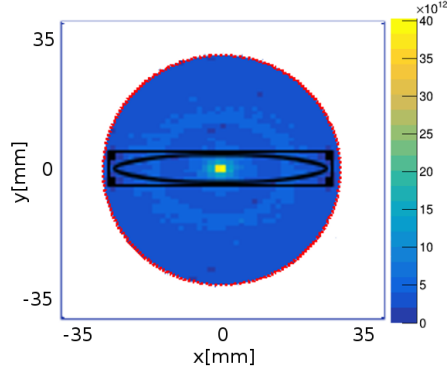


Figure 5.3: The beam spacial profile hitting the targets (black ellipse) enclosed in their frames (black rectangle) at 100 meters away from the GF interaction point. The color scale shows the flux [$\gamma/\text{s}/\text{mm}^2$] on the orthogonal plane (x, y) .

pute the energy deposited in He, while they are stopped, using ATIMA model [69] inside GEANT4 framework. In fig.5.4 is shown the energy and mass distributions of the produced and released ions.

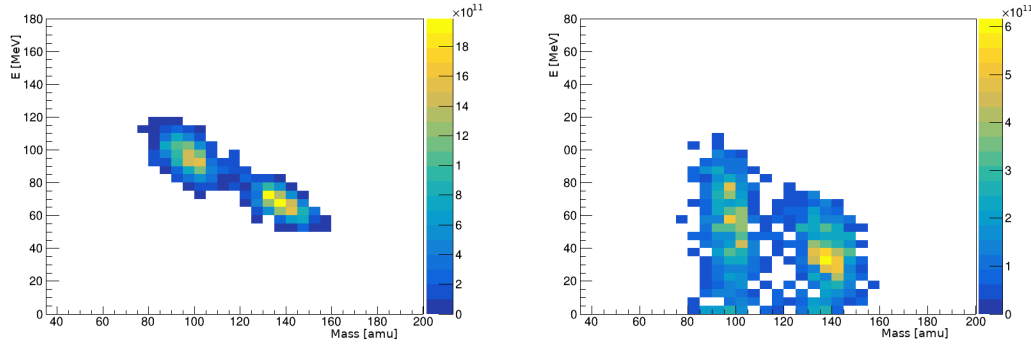


Figure 5.4: Ions energy at the production point (left) and when released from the targets into the gas (right). The color scale shows the intensity [ions/s] for the produced and release ions.

The GEANT4-simulated yield of the ions released in the gas is 10^{12} ions/second which is orders of magnitude higher than in the current RIB facilities, but this high rate produces significant space charge inside the cell. While ions are stopped, they deposit their energy in the gas mainly by ionization, creating the He^+ ions that arrange themselves into He_3^+ trimers. The fission fragments have a mean kinetic

energy of 39.8 MeV when they escape the targets, and thus each stopped ion is producing about 10^6 $\text{He}^+ \text{-e}^-$ pairs, taking 41 eV [54] as the He ionization potential. The total charge of the He_3^+ ions accumulated for 1 second at the full beam is then about 1 mC.

5.1.5 Extraction efficiency estimation

We estimate the ions extraction efficiency using SIMION [70] simulations of a slice of the HADO-CSC, a $25 \text{ cm} \times 25 \text{ cm}$ full orthogonal plane, 3.3 cm thick, in which we have added one circular target with the corresponding frame (fig.5.5). The results are relevant for the whole CSC which can be seen as being made up of 54 identical parts as the one simulated.

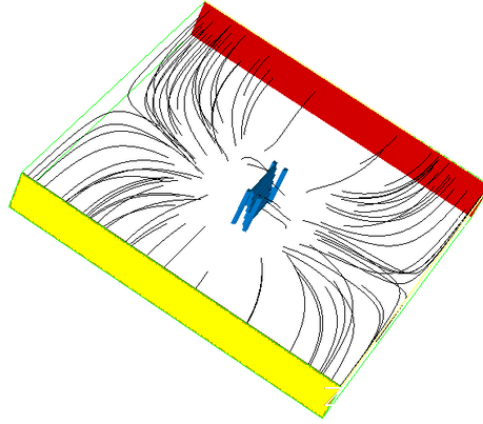


Figure 5.5: The SIMION geometry consisting of the full orthogonal plane of the CSC, thick enough to accommodate one UO_2 circular target ($D = 30 \text{ mm}$) embedded in a AlMg_3 , $35 \text{ mm} \times 35 \text{ mm}$ square frame inclined at 10° with respect to the beam axis and secured with 4 metal rods ($D = 3 \text{ mm}$) in the corners. The external field is created between the extraction electrode (red), which is put on a negative potential to attract the positive ions, and the grounded electrode (yellow). The target system (blue) is put at half of the potential of the extraction electrode in order to obtain a smooth field and suppress the very near He_3^+ ions.

We proceed for static simulations using variations of the extraction electric field from 100 V/cm up to 500 V/cm, which is approximately a half of the Paschen's Law limit, and superimposing the full space charge imported from GEANT4. As expected, the formed He_3^+ cloud density shown in fig.5.6 is focused in the center

of the cell in the vicinity of the target system, where the ions have most of energy and a higher spacial density.

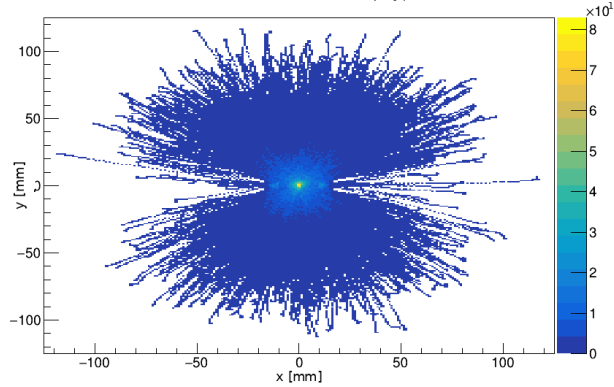


Figure 5.6: He_3^+ ions/second/ mm^2 flux spacial distribution, in the orthogonal plane, generated due to fission fragments energy deposition in the gas.

Due to this high positive charge created in the center, the ions are pushed and accelerated towards the cell walls with high velocity, with behaviour shown in fig.5.7.

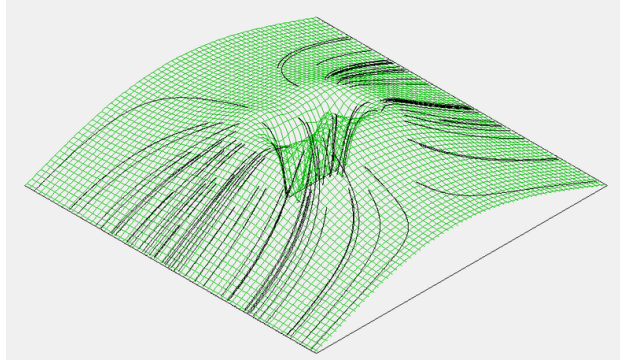


Figure 5.7: The static simulation with a small number of ions showing the extraction behavior due to the high space charge density in the center of the CSC on top of the total electric field created (external plus space charge).

To prevent the ions from penetrating the cell wall, and thus loose them, strong but short repulsive electric fields are used, generated by radio-frequency circuits, called the RF carpets [68]. The current state-of-the-art radio-frequency carpets

(RFCs) can catch ions that have a perpendicular velocity lower than 50 m/s [71]. In our static simulation, the high space charge, which is located mostly in the center, acts as an electrode with high potential that pushes the ions towards the walls. An important fraction of the ions, about 19%, is estimated to hit the extraction electrode, but due to the high velocity (more than 5 km/s) they cannot be stopped and caught by the RF field, and thus escape by penetrating the RF carpet that leads to almost no extraction. The need to lower the space charge while keeping a maximal ion yield, led to the idea of chopping the beam in such a way that the space charge is accumulated for much less time and then evacuated before the next bunch. The SIMION estimation for the extraction time is less than 1 ms, thus the proposed solution is to chop the beam in 1 ms on and 1 ms off bunches, resulting in a space charge reduction by 3 orders of magnitude, while the ion yield is lower just by a factor of 2 to the rate of 0.5×10^{12} ions/second. This important reduction of the space charge is due to the fact that the ionization is accumulated for just 1 ms versus 1 s, and then in the next 1 ms (when the beam is off) there is time that the charge is fully evacuated and the cell is ready for the next bunch. The ion yield is cut just by half because the ion production takes place with the full beam intensity for periods equal to the paused period. With a total space charge of $10 \mu\text{C}$, corresponding to the described chopped beam, we have performed full static and also dynamic, particle-in-cell (PIC) SIMION simulations with the up and down space charge and external extraction field variations in order to find the maximum yield for the extracted ions (fig.5.8).

In this range of the space charge, the mean velocity of the ions is near the RF carpet limit of 50 m/s and for the optimum case the velocity is below this limit. The external field plays the role of guiding the ions towards extraction and usually a stronger field is preferred for improving the extraction time and efficiency. In the presented case, the ions are strongly pushed to the extraction electrode by the high centered density of space charge, thus a strong external field would increase the velocity of the ions above the 50 m/s limit when hitting the extraction RF carpet. The best extraction efficiency of about 8% has been obtained using a relatively low, 10 V/cm, external field combined with the $0.8 \mu\text{C}$ total space charge accumulated in the cell, corresponding to a beam bunch time profile of 0.8 ms on and 1 ms off.

An even lower external field could not be used due to the electron-ion recombination effect.

The high ion yield of about 7.2×10^{10} ions/second, extracted from the proposed setup, permits the measurement and analysis of rare exotic nuclei, which are produced with a very low cross section, and covers both the $N = 50$ and $N = 82$

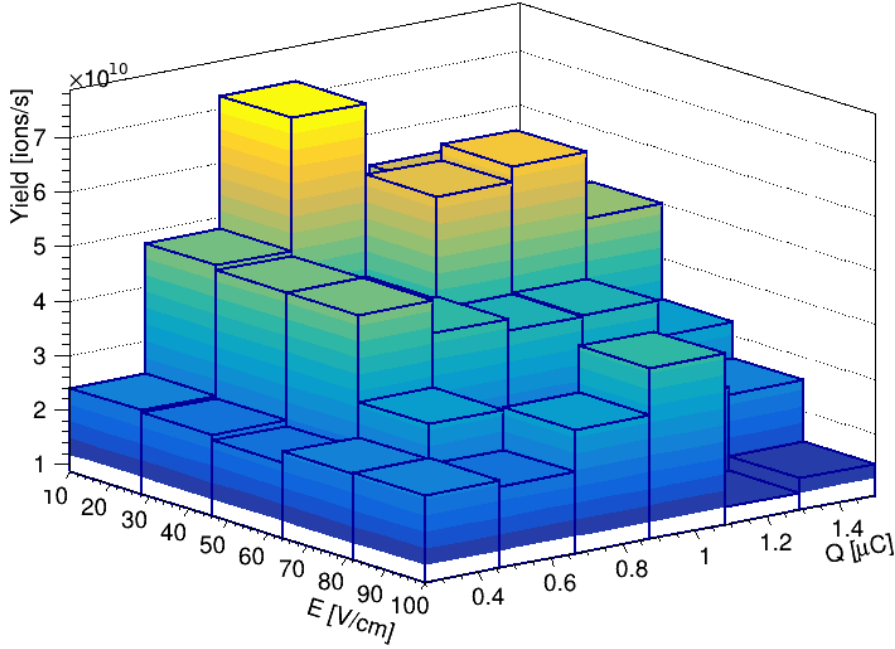


Figure 5.8: The total extracted ion yield for variations of the external electric field (E) and the total space charge in the cell (Q).

r-process waiting points. fig.5.9 is generated using a fit of the distribution of the ions being released from the targets resulting from the GEANT4 simulations, normalized to the extracted ions/s yield presented as the optimum case in this work with the assumption that the extraction process is isotope-independent. The yield is stopped at 1 ion/s, where standard mass and decay spectrometry measurements are easily performed. The *r*-path region [72] shown in fig.5.9 with red lines is one of the several theoretical scenarios developed to date. A more detailed, typical isotopes yield comparison with ISOLDE [73], FRIB [74] and CARIBU [75] is presented also in Table 5.1.

5.1.6 RIB yields available for measurement

The proposed ELISOL type setup at the GF produces ion yields of the order 10^{12} ions/second via photo-fission process of the high flux γ -rays impinging on multiple thin actinide targets. This production rate is obtained with about 6×10^{15} gammas/second hitting the 54 targets and correlated with the proposed solutions

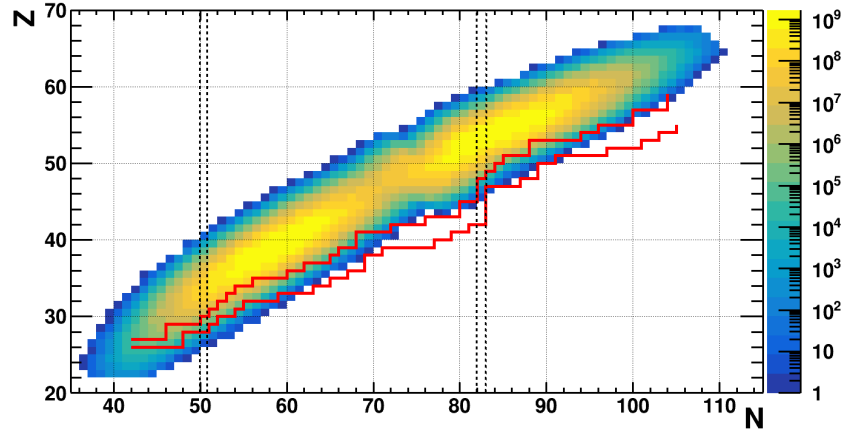


Figure 5.9: The extracted ions-yield (side color scale in ions per second) as a function of proton number (Z) and neutron number (N) isotope distribution chart and the r -process (red line) [72]. The black dotted line points out the $N=50$ and $N=82$ r -process waiting points.

Table 5.1: Yield comparison of several common isotopes of interest in ions/second for GF, FRIB and CARIBU and ions/ μC for ISOLDE with a typical $2\mu\text{A}$ proton beam current [76].

	^{76}Co	^{78}Ni	^{110}Zr	^{132}Sn	^{136}Sn	^{160}Ce
GF [ions/s]	8×10^3	3×10^4	178	7×10^7	9×10^4	238
ISOLDE [ions/ μC]	NA	NA	NA	3×10^8	4×10^3	NA
FRIB [ions/s]	0.1	7	36	10^6	29	0.1
CARIBU [ions/s]	NA	NA	NA	2.4×10^3	NA	NA

to lower the space charge effect are resulting in extracted ion yields of about 7.2×10^{10} ions/second which is significantly higher than the current RIB facilities. Although the assumption for isotope-independent extraction is not quite precise, the yield distribution which is presented in fig.5.9 demonstrates the potential of the technique for studies of most exotic neutron-rich nuclei, lying far away from the valley of β -stability. Another key advantage of the technique is that due to the ultra fast electric field extraction, estimated to be in the range of a few milliseconds, thus properties of the very short lived nuclei became available for measurements.

5.2 Physics opportunities with RIBs at Gamma Factory

Starting from the work and results presented in the previous section, the decay process has been applied, by taking into account the half-lives and decay modes that take place during ions extraction, transport and measurement. The available yield of each isotope is altered in two ways, on one hand it is decreasing due to the decay and on the other hand it is populated due to the decay of the mother nuclei upstream on the decay chain, before the isotope separation started. Information about the decay processes and half-lives was extracted from AME [77] [78], though for some exotic isotopes produced this information is not available. In this later case, the decay process was not applied and thus the final yields for those isotopes are undetermined. In fig.5.10 estimated yields are presented for isotopes that are available after the extraction, transport and measurement processes. This time was considered to be around 40 ms. The yield threshold considered is one particle per hour corresponding to a standard acceptable rate that permits mass measurements.

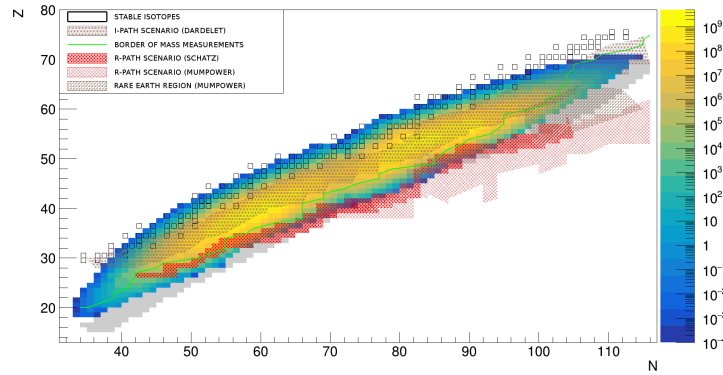


Figure 5.10: Yields (color axis) greater than one per hour for isotopes that are extracted and survived the 40 ms time to and in the measurement station. Black squares represents stable isotopes and the green line shows the limit of performed mass measurements nowadays. The isotopes colored in gray are cases in which the final yield could not be estimated due to the lack of decay and life-time information. The brown stars represents proposed area of the *i*-process from [79], light red and dark red hashed areas show *r*-process scenarios from [72], [80] and brown step-like markers show a rare Earth elements formation area from [80]

The neutron separation energy $S_n(N, Z) = B(N, Z) - B(N - 1, Z)$ is an important parameter in the calculation of the r -process in nucleosynthesis models, which was discussed in the previous sections, mainly because the radiative neutron capture cross section decreases exponentially with $S_n/k_B T$. This makes the reaction networks highly sensitive to its value along the r -path, especially around the waiting points. Nonetheless, the large majority of the necessary nuclear masses have not been measured [80] and will be difficult to reach even at future RIB facilities. In this context, the extent of the coverage of the various r -path scenarios with the proposed GF facility is outstanding, as shown in Fig. 5.10.

Mass measurements close to the r -path in the rare earth region are crucial in astrophysical reaction network calculations due to the significant contribution of these nuclei in the β -decay component. Fig. 5.10 shows the striking increase in the number of measured masses at the GF, with 5-7 new masses for each light rare earth element and up to 7-9 new masses for each heavy rare earth element.

For validation purpose, a series of isotopes chain yields made available by the Gamma Factory are compared with yields generated by current state of the art RIBS facilities as: CARIBU (ANL) [20], ISOLDE (CERN) [22] and FRIB (MSU) [81].

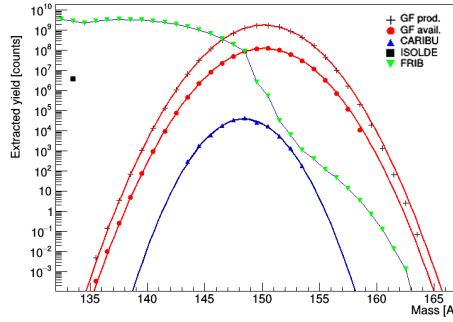


Figure 5.11: Mass chain yield of Ce isotopes shown for several RIBs (indicated in the figure legend).

In fig. 5.11 the Cerium (Ce) isotopic chain yields are presented function of their mass. For the Gamma Factory, the red dots represents the survival yields after the 40 ms estimated for extraction, transport and measurement while the larger red curve fitting the black stars is showing the GF production yields. The blue markers [75] and eye guiding fit show yields available for measurement at CARIBU facility while the green triangles [74] show the yields available at FRIB.

Gamma factory, makes available about two more masses in the case of the Cerium chain and up to 5-9 new masses throughout the medium and high mass nuclei ($A \approx 70 - 170$). As previously discussed, study of nuclei around closed shells are relevant for nuclear structure understanding e.g. ^{78}Ni ($Z = 28, N = 50$) thus a comparison yield plot has been performed for the Nickel chain, shown in the right part of fig.5.12. In the left part of fig.5.12 Cobalt isotopes yields are plotted in comparison as an astrophysical importance example nuclei. In both Nickel and Cobalt chains, the Gamma Factory is making available considerably more isotopes in the far neutron-rich side.

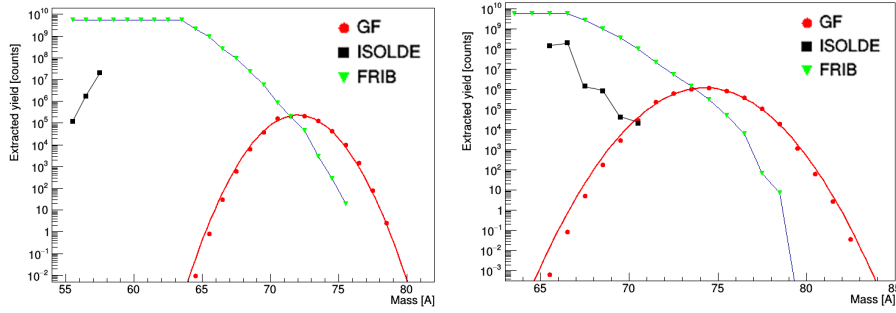


Figure 5.12: Mass chain yield of Co isotopes (left frame) and Ni isotopes (right frame) shown for several RIBs (indicated in the figure legends).

This work demonstrates that new exotic neutron-rich isotopes can be produced at the Gamma Factory and made available for different types of measurements that have important implications in many physics cases. Although these results are based on simulations, the considerable improvement that is discussed here gives confidence that the radioactive ion beam facility (RIB) at the Gamma Factory should be further followed for its important potential.

This chapter is based on the publication "Radioactive ion beam production at the Gamma Factory", *Ann. Phys. (Berlin)*, 2100207, 2021 in which the thesis author is the writer and first-author and also on the "Physics opportunities with the Gamma Factory", paper in preparation by the author.

Chapter 6

Conclusions and outlook

In this work are presented the methods and challenges of the most important processes of a radioactive beam facility, from the production of the radioactive isotopes, their extraction, beam formation, measurements of their properties and the scientific impact of such an endeavor. The solutions proposed here might offer the possibility to further our knowledge in fundamental nuclear physics, astrophysics and enlarge the application of radioactive ions.

Firstly the general theory of the nuclear fission process is presented, studies of this process having impact on our understanding of the nuclear structure and playing an important role in energy generation applications such as fission nuclear reactors. The fission process is also proposed as an efficient radioactive ions production method, studies and optimization of this process being extensively performed as part of this thesis.

The second chapter introduce the place of exotic, neutron rich, radioactive ions in the grand scheme of the Universe creation and evolution.

Many of these elements are believed to be created in fairly complex processes that imply series of interaction and decays that take place in special conditions, thus in order to confirm and better understand these mechanisms, one needs to recreate them here on Earth.

In the pursuit of understanding the fission process, an experimental study of the prompt fission gamma rays is performed and presented as original work in this thesis in the third chapter. A procedure for unfolding the measured data from the detector response function is implemented throughout the study.

The fourth chapter presents another original work [40] that has the goal of optimizing the production of radioactive, neutron-rich isotopes through a photo-fission mechanism taking place inside actinide targets, experimental setup pro-

posed to be developed at ELI-NP, Romania. The freshly produced isotopes that possess high kinetic energy, are then thermalized inside a cryogenic stopping cell and then extracted using electric fields. The radioactive ion beam is formed with the help of a radio-frequency quadrupole (RFQ) and further cleaned with a multi-reflection time-of-flight mass spectrometer (MR-TOF). The new design of the setup is allowing the production and extraction of new elements, specially in the refractory region, isotopes that pose great challenge to be made available in the current generation facilities.

The fifth chapter continues with an original work [42] that proposes a case study of a new radioactive beam facility with the isotope production being based on fission generated by high intensity photon beams coming from the Gamma Factory (GF) facility proposed at CERN that impinge on thin actinide foils. Even though GF is in the project phase, this work clearly demonstrates the opportunity to produce radioactive beams with intensities that allow measurement of 2 to 9 more isotopic masses per each chain. In the last section of chapter five, the scientific impact of such possible measurements is presented alongside with different comparison with current state of the art radioactive ion beam facilities to allow an overview and placement of the proposal in the field. The thesis concludes by demonstrating that the new available isotopes reach areas of importance for astrophysics (*r*-path modeling) but also for nuclear structure understanding making available measurements of properties like masses, decay rates, dipole magnetic moments, charge radii, and so on, for new isotopes in the far exotic neutron-rich side of the Segre chart.

List of abbreviations

AGB	Asymptotic Giant Branch
ALTO	Accélérateur Linéaire et Tandem à Orsay, France
AME	Atomic Mass Evaluation
ANL	Argonne National Laboratory
ARIEL	Advanced Rare IsotopE Laboratory
ATIMA	Atomic Interaction with Matter
CAIN	BeamBeam Interactions framework
CARIBU	The Californium Rare Isotope Breeder Upgrade
CEC	Charge Exchange Cell
CERN	Conseil Européen pour la Recherche Nucléaire
CLS	Collinear Laser Spectroscopy
CSC	Cryogenic Stopping Cell
DAQ	Data Acquisition System
ELI-NP	Extreme Light Infrastructure - Nuclear Physics
ELISOL	Extreme Light Infrastructure Isotope Separator On-Line
FAIR	Facility for Antiproton and Ion Research in Europe
FRS	Fragment Separator
FRIB	Facility for Rare Isotope Beams
FWHM	Full Width at Half Maximum
GANIL	Grand Accélérateur National d'Ions Lourds, France
GDR	Giant Dipole Resonance
GEANT4	Geometry And Tracking framework

GIF23U Gamma Induced Fission of ^{238}U

GSi Gesellschaft für Schwerionenforschung, Germany

GF Gamma Factory

HADO-CSC High Areal Density, Orthogonal extraction Cryogenic Stopping Cell

IFIN-HH Institutul Național de Cercetare Dezvoltare pentru Fizică și Inginerie Nucleară "Horia Hulubei"

ISAC Isotope Separator and Accelerator

ISOL Isotope Separation On-Line

ISOLDE Isotope Separation On-Line Device

ISOLTRAP Isotope Separation On-Line Trap

JRC Joint Research Centre

JYFL Jyväskylän yliopiston fysiikan laitos, Finland

KEK Kō Enerugi Kasokuki Kenkyū Kikō Japan

LCB Laser Compton-Backscatter

LIGO Laser Interferometer Gravitational-Wave Observatory

LHC Large Hadron Collider

MIDAS Multi Instance Data Acquisition System

MR-TOF Multi Reflection Time of Flight

MSU Michigan State University

MTA EK Magyar Tudományos Akadémia Energiatudományi Kutatóközpontban,
Hungary

NMR Nuclear Magnetic Resonance

NSCL National Superconducting Cyclotron Laboratory

PIC Particle In Cell

PFGS Prompt Fission Gamma-ray Spectra

PSI Partially Stripped Ions

RFC Radio-Frequency Carpets

RFQ Radio-Frequency Quadrupole

RIB Radioactive Ion Beam

RIBF Radioactive Isotope Beam Factory

RIKEN Rikagaku Kenkyusho, Japan

ROOT Rapid Object-Oriented Technology framework

RMS Root Mean Square

SARAF The Soreq Applied Research Accelerator Facility

SIMION Ion and Electron Optics Simulator software framework

TRIUMF TRI-University Meson Facility

TOF Time Of Flight

VEGA The Variable Energy Gamma System

Bibliography

- [1] The discovery of nuclear fission. <https://www.mpic.de/4469988/die-entdeckung-der-kernspaltung>. Accessed: 2022-May-04.
- [2] L. Csige et al. *Phys. Rev. C*, 80:18–19, 2009.
- [3] J. Sadhukhan et al. *Frontiers in Physics*, 2020.
- [4] N. Schunck et al. *Prog. Part. Nucl. Phys.*, In press, 2022.
- [5] G. Vladuca. University of Bucharest, 1990.
- [6] B. Mei et al. *Phys. Rev. C*, 96:064610, 2017.
- [7] A. Oberstedt et al. *Phys. Rev. C*, 87, 2013.
- [8] A. Frebel. Princeton University Press, 2015.
- [9] E.M. Burbidge et al. *Rev. Mod. Phys.*, 29:547, 1957.
- [10] A.G.W. Cameron. *Chalk River Rep. CRL*, 41, 1957.
- [11] T. Kajino et al. *Prog. Part. Nucl. Phys.*, 107:109–166, 2019.
- [12] C. J. Horowitz et al. *J. Phys. G: Nucl. Part. Phys.*, 46, 2019.
- [13] S. E. Woosley et al. *Rev. Mod. Phys.*, 74 (4):1015–1071, 2002.
- [14] J. J. Cowan et al. *Rev. Mod. Phys.*, 93, 2021.
- [15] R. C. Duncan et al. *Astrophys J. Lett.*, 392:9–13, 1992.
- [16] R. A. Hulse et al. *Astrophys J.*, 195:51–53, 1975.
- [17] B. P. Abbott et al. *Phys. Rev. Lett.*, 116, 2016.

- [18] B. P. Abbott et al. *Rep. Prog. Phys.*, 72, 2009.
- [19] B. P. Abbott et al. *Phys. Rev. Lett.*, 119, 2017.
- [20] G. Savard et al. *Nucl. Instrum. Methods B*, 266:4086, 2008.
- [21] A. Sen et al. *Nucl. Instrum. Methods B*, 376:97, 2016.
- [22] D. Voulot et al. *Nucl. Instrum. Methods B*, 266:4103, 2008.
- [23] W.R. Plaß et al. *Nucl. Instrum. Methods B*, 317:457, 2013.
- [24] H. Geissel et al. *Nucl. Instrum. Methods B*, 70:286–297, 1992.
- [25] P. Delahaye et al. *Nucl. Instrum. Methods B*, 463:339, 2020.
- [26] A. Gade and C. Konrad Gelbke. *Scholarpedia*, 5(1):9651, 2010.
- [27] J. Aysto et al. *Nucl. Phys. A*, 693:477, 2001.
- [28] T. Sumikama et al. *Nucl. Instrum. Methods B*, 376:180, 2016.
- [29] Y. Blumenfeld et al. *Phys. Scr. T*, 152:014023, 2013.
- [30] M. Cheikh Mhamed et al. *Nucl. Instrum. Methods B*, 266:4092, 2008.
- [31] C. Babcock et al. *Nucl. Instrum. Methods B*, 463:464, 2020.
- [32] M. Lindroos. *Proceedings of EPAC 2004, Lucerne, Switzerland*, 2004.
- [33] D. J. Morrissey. *Phil. Trans. R. Soc. Lond. A*, 356, 1998.
- [34] I. Mardor et al. *Phys. Rev. C*, 103, 2021.
- [35] T. Dickel et al. *J. Phys.: Conf. Ser.*, 1668, 2020.
- [36] D. T. Yordanov et al. *JINST*, 15, 2020.
- [37] G. V. Turturica et al. *Eur. Phys. J. Plus*, 135, 2020.
- [38] P.-A. Söderström et al. *JINST*, 14, 2019.
- [39] P.-A. Söderström et al. *Nat. commun.*, 11, 2020.
- [40] D. Nichita et al. *U.P.B. Sci. Bull. A*, 82:297, 2020.

- [41] P. Constantin et al. *Nucl. Instrum. Methods B*, 461:130–132, 2019.
- [42] D. Nichita et al. *Ann. Phys. (Berlin)*, 2100207, 2021.
- [43] S. Schmitt. *EPJ Web of Conferences*, 137, 2017.
- [44] T. Belgia. *Phys. Rev. C*, 74:024603, 2006.
- [45] A. N. Tikhonov. *L'Academie des Sciences de l'URSS*, 1943.
- [46] S. Schmitt. *JINST*, 7, 2012.
- [47] T. Adye. *Proceedings of the PHYSTAT 2011 Workshop, CERN*, 2011.
- [48] R. Brun. *Nucl. Inst. and Meth. in Phys. Res. A*, 389:81–86, 1997.
- [49] J. Friedman. *Proc. of the 1974 CERN School of Computing*, 1974.
- [50] N.V. Zamfir. *Nuclear Physics News*, 34:25, 2015.
- [51] D.L. Balabanski et al. *Europhys. Lett.*, 28001:117, 2017.
- [52] D. Ursescu et al. *Proc. SPIE*, 8780, 2013.
- [53] H.R. Weller et al. *Rom. Rep. Phys.*, 68:447, 2016.
- [54] P. Constantin et al. *Nucl. Instrum. Methods B*, 397:1, 2017.
- [55] D.L. Balabanski et al. *Rom. Rep. Phys.*, 68:621, 2016.
- [56] P. Constantin et al. *Nucl. Instr. Meth. Phys. Res. B*, 372:78–85, 2016.
- [57] T. Dickel et al. *Nucl. Inst. and Meth. in Phys. Res. B*, 376:216, 2016.
- [58] S. Agostinelli et al. *Nucl. Instrum. Meth. A*, 506:250–303, 2003.
- [59] C. Donzaud et al. *Eur. Phys. J. A*, 1:407, 1998.
- [60] S. Pomme et al. *Nucl. Phys. A*, 560:689, 1993.
- [61] Mieczysław Witold Krasny, 2015. arXiv:1511.07794 [hep-ex].
- [62] H.R. Weller et al. *Progr. Part. Nucl. Phys.*, 62:257, 2009.
- [63] Wiesław Płaczek. GF-CAIN, 2020. code to be obtained from the author.

- [64] M. W. et al. (Gamma Factory Study Group) Krasny. Letter-of-Intent (LoI), CERN-SPSC-2019-031, SPSC-I-253, 2019.
- [65] Kaoru Yokoya et al. CAIN, version 2.42. <https://ilc.kek.jp/yokoya/CAIN/Cain242/>, 2011.
- [66] J. T. Caldwell et al. *Phys. Rev. C*, 21:1215, 1980.
- [67] Daniel Kasen et al. *Nature*, 551:80, 2017.
- [68] M. Wada et al. *Nucl. Instrum. Methods B*, 204:570, 2003.
- [69] H. Weick et al. *Nucl. Instrum. Methods B*, 193:1, 2002.
- [70] D. Manura and D. Dahl. Simion 8.0 manual, Sci. Instrum. Serv. Inc., 2008.
- [71] A. Rotaru et al. *U.P.B. Sci. Bull. A*, 81:197, 2019.
- [72] H. Schatz and K. Blaum. *Europhys. News*, 37:16, 2006.
- [73] http://isoyields-classic.web.cern.ch/query_tgt.htm.
- [74] <https://groups.nsl.msui.edu/frib/rates/fribrates.html>.
- [75] <https://www.anl.gov/atlas/caribu-beams>.
- [76] Maria J. G. Borge and Bjorn Jonson. *J. Phys. G: Nucl. Part. Phys.*, 44, 2017.
- [77] W. J. Huang et al. *Chinese Phys. C*, 45, 2021.
- [78] AMDC - atomic mass data center. <https://www-nds.iaea.org/amdc/>.
- [79] L. Dardelet et al. *Proceedings of Science - NIC XIII*, 204, 2015.
- [80] M. R. Mumpower et al. *Prog. Part. Nucl. Phys.*, 86:86–126, 2016.
- [81] C. Wrede. *EPJ Web of Conferences*, 93, 2015.